Integrated Coastal Subsidence Analysis Using InSAR, LiDAR, and Land Cover Data

Wen Zhong[1, 2], Tianxing Chu[1, 2], Philippe Tissot[1], Zhenming Wu[3], Jie Chen[4], Hua Zhang[5, *]

[1] Conrad Blucher Institute for Surveying and Science, Texas A&M University-Corpus Christi, Corpus Christi, TX 78412, USA.

[2] Department of Computing Sciences, College of Science and Engineering, Texas A&M University-Corpus Christi, Corpus Christi, TX 78412, USA.

[3] Department of Meteorology, University of Reading, Reading, Berkshire, RG6 6BB, UK.

[4] State Key Laboratory of Cryosphere Science, Northwest Institute of Eco-Environment and Resources, Chinese Academy of Sciences, Lanzhou 730000, China.

[5] Department of Engineering, College of Science and Engineering, Texas A&M University-Corpus Christi, Corpus Christi, TX 78412, USA.

Abstract

Land subsidence is an important cause of relative sea-level rise along the Gulf Coast. There is a lack of effective monitoring of coastal subsidence with high accuracy and high spatial resolution for improving coastal risk assessment and mitigation. This study is the first attempt to integrate satellite interferometric synthetic aperture radar (InSAR) and airborne LiDAR

methods to investigate the spatiotemporal pattern of coastal subsidence. The study area is around Eagle Point, Texas, a region known for its fast rate of relative sea-level rise in recent decades. From 2006 to 2011, the line-of-sight velocities were up to −33 mm/year based on ascending ALOS-1 PALSAR-1 images. From 2016 to 2021, the vertical velocities were up to −34 mm/year based on ascending and descending Sentinel-1 images. Additional details of the subsidence pattern were revealed by incorporating the surface difference derived from 1-m airborne LiDAR results. Comparisons of the InSAR-derived velocities from image time series and the LiDAR-derived surface changes from time-lapsed observations were conducted at different spatial levels with linkages to land cover patterns and topography. The results showed that local subsidence rates could vary significantly below the spatial resolution of InSAR results, indicating a valuable role of airborne LiDAR results in extending InSAR results to parcel and building levels and explaining subpixel uncertainties. Also, subsidence appeared stronger in vegetated areas than in developed areas and negatively correlated with surface imperviousness. The magnitude of subsidence was not correlated with elevation along selected transect lines. Overall, this study demonstrated the benefits of combining InSAR results with other geospatial datasets to characterize coastal subsidence. In particular, the high vertical accuracy InSAR results and the high spatial resolution airborne LiDAR results could be complementary, highlighting the necessity of multi-resolution data fusion to support studies on coastal flood vulnerability, infrastructure reliability, and erosion control.

Keywords: Land subsidence, Coastal regions, InSAR, Airborne LiDAR, Land cover

1. Introduction

More than 600 million people, or 10 % of the world's population, live in low-lying coastal areas below 10 m in elevation (Neumann et al. 2015). These coastal areas are unique ecosystems that offer habitats for many species and provide essential services to human society. The market value of marine and coastal resources was estimated at $3 trillion annually as the year of 2015, accounting for 5% of global gross domestic product (Global Ocean Commission 2014). Over the past decades, relative sea-level rise (RSLR) has been identified as a significant threat to many coastal areas. It is exacerbating a variety of environmental and ecological problems such as coastal flooding (Ezer and Atkinson 2014), wetland loss (Schuerch et al. 2018), and coastal erosion (Leatherman et al. 2000), endangering local ecosystems and communities. RSLR is the combined effect of sea-level rise and land subsidence. Potential causes of sea-level rise include meltwater from glaciers and ice sheets, thermal expansion of seawater, and transfers of water from storage on land to sea (Frederikse et al. 2020; Meredith et al. 2019). Land subsidence is associated with natural and human causes at local or regional scales, such as groundwater withdrawal, oil and gas extraction, soil compaction, fault growth, tectonic activities, and other natural processes (Coplin and Galloway 1999).

The contribution of land subsidence to RSLR is particularly significant along the Texas Gulf Coast (Coplin and Galloway 1999). For example, the contribution of land subsidence was estimated to be 76-85% of RSLR from 1909 to 1992 and decreased to 30% in 2018 at tide gauge Galveston Pier 21, Texas (Liu et al. 2020), over an area known for significant

63 subsidence (Miller and Shirzaei 2019; Qu et al. 2015). Driven by growing concerns about the
64 effect of land subsidence on coastal flooding, shoreline erosion, and fault movement (Coplin
65 and Galloway 1999; Miller and Shirzaei 2021), there is an urgent need for effective
66 characterization of land subsidence to improve risk management strategies for Texas coastal
67 areas.

68 Traditional efforts of subsidence analysis rely on ground-based techniques. For example,
69 geodetic surveying methods such as leveling have been used to measure the vertical change of
70 the ground surface at the local scale. Extensometers have also been used to measure aquifer
71 compaction and expansion for estimating subsidence around wells (Huang et al. 2012), but
72 the low spatial coverage of extensometers hinders the understanding of the spatial variations
73 of regional subsidence. Another method for subsidence monitoring is the global navigation
74 satellite system (GNSS) (Wang et al. 2017). In particular, continuous GNSS stations, such as
75 NOAA's continuously operating reference station (CORS) network, can offer positioning
76 observations with high accuracy, but the results are only valid for a limited area around the
77 stations.

78 Geodetic remote sensing techniques can continuously monitor the dynamic displacement
79 of the ground surface and provide a new means to quantify land subsidence. In particular, the
80 interferometric synthetic aperture radar (InSAR) has been proven to be an effective tool to
81 map land subsidence with centimeter-to-millimeter accuracy over a large geospatial extent
82 (Bürgmann et al. 2000). It compares two or more synthetic aperture radar (SAR) images that
83 are collected at different times over the same region to quantify the change of ground surface.

84 Due to the growing availability of high-quality SAR datasets, InSAR has been increasingly
85 used in coastal subsidence studies (Dixon et al. 2006; Wang et al. 2012). For example, Qu et
86 al. (2015) mapped the line of sight (LOS) subsidence in the Galveston-Houston region, Texas,
87 using InSAR based on ERS, Envisat ASAR, and ALOS-1 PALSAR-1 images from 1993 to
88 2011. Miller and Shirzaei (2021) generated the vertical land subsidence rate over this area
89 based on ALOS-1 PALSAR-1 and Sentinel-1 images between 2007 and 2019 and GNSS
90 measurements which provided the horizontal component of the motion for the same period.
91 Results of these InSAR-based subsidence studies typically have a horizontal spatial resolution
92 in tens-of-meters. In comparison, airborne LiDAR (Light Detection and Ranging) could offer
93 insights at a higher spatial resolution (up to 1 m), although with a lower vertical accuracy
94 (10−15 cm). Airborne LiDAR is an aerial mapping technology that integrates LiDAR and
95 aerial platforms (e.g., a drone, plane, or helicopter) to collect the three-dimensional (3D) point
96 cloud of the earth's surface for the generation of digital terrain models (DTM) or digital
97 elevation models (DEM). Recent advances in drone technology have particularly promoted
98 the applications of airborne LiDAR. Integrating InSAR and airborne LiDAR methods can
99 potentially study coastal subsidence with high accuracy and high spatial resolution.
100 The objectives of this study are to 1) quantify the subsidence rates in a Texas coastal area
101 from 2006 to 2021 using the small baseline subset (SBAS) InSAR method, and 2) compare the
102 InSAR results to the high-resolution land surface differences derived from multitemporal
103 airborne LiDAR data, and 3) investigate the relationships between subsidence and the patterns
104 of land cover and topography. This study aims to explore a complementary relationship

between the high accuracy InSAR results and the high spatial resolution airborne LiDAR results in supporting coastal subsidence studies.

2. Study Area

The study area is a 520 km^2 area around Eagle Point in Texas, located between 29°20'N and 29°34'N and between 95°5'W and 94°52'W (Fig. 1). The land cover is dominated by a mixture of coastal prairie, urban areas, and an industrial zone of oil and gas facilities in the southeast area. Elevation ranges from −4.43 m to 17.05 m with an average slope of 0.18°. Records from the Eagle Point Tide Gauge Station show an RSLR rate of 13.7 mm y^{-1} from 1993 to 2017 (Fig. 1b). A possible cause is the withdrawal of groundwater from the Chicot, Evangeline, and Jasper aquifers, all components of a broader Gulf Coast aquifer system, to meet the increasing industrial and municipal water demands from the Galveston area. Oil and gas extraction, and surface fault activities could also contribute to the land subsidence here (Coplin and Galloway 1999; Qu et al. 2015).

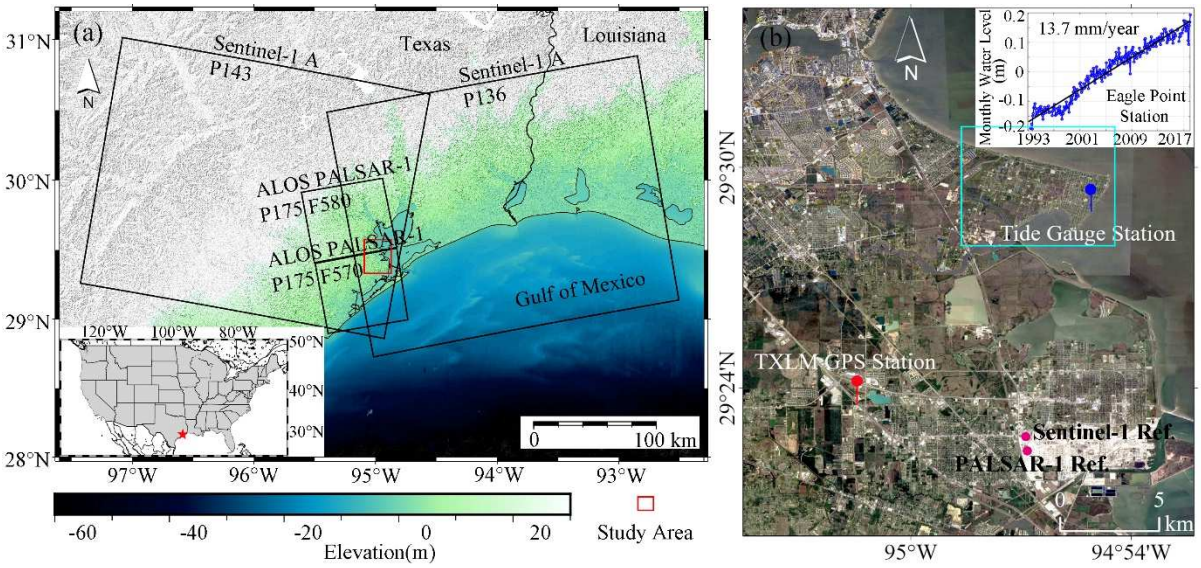

Figure 1. Study area: (a) SAR data coverage (black squares) over the elevation map around the study area (red square); (b) a Google Earth image of the study area and the monthly mean RSLR observed at the Eagle Point Tide Gauges Station (blue marker) from 1993 to 2017. Red marker shows the location of the TXLM GPS station, and magenta dots denote the location of the reference points for Sentinel-1 and ALOS-1 PALSAR-1 image processing.

3. Methods and Materials

3.1 Overview

This study combined InSAR, airborne LiDAR, GPS, and land cover data to investigate the spatiotemporal pattern of coastal land subsidence and its relation to different land cover and topography, consisting of several steps (Fig. 2). First, three stacks of SAR images were used to obtain the LOS subsidence velocities, i.e., two orbits from Sentinel-1 and one from ALOS-1 PALSAR-1. LOS velocities in both ascending and descending geometries of Sentinel-1 were utilized then to generate the projections onto the vertical and east-west

horizontal directions under the assumption of zero north-south motion. Second, this study generated a 1-m land surface difference map from two temporal airborne LiDAR point cloud data to compare and complement InSAR results. Third, the InSAR results were overlapped with land cover data to examine the occurrence of subsidence in different land cover categories, and its relationship with percent surface imperviousness. Finally, InSAR results and LiDAR DEM were combined in a profile analysis to investigate the pattern of subsidence along selected transections and highways across the study area. Highways are often a focus of mitigation and response studies for flooding risk management, as land subsidence along low-lying highway sections could exacerbate the inundation risk.

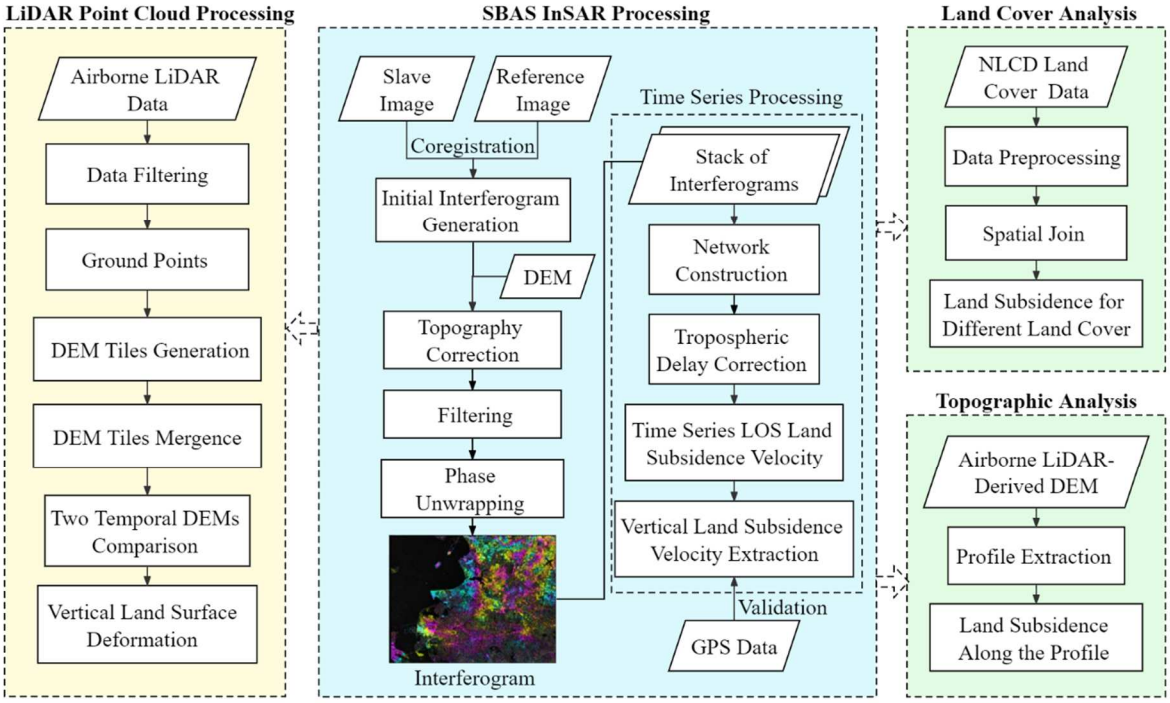

Figure 2. Research framework.

147 **3.2 InSAR-Based Subsidence Analysis**

148 **3.2.1 SAR Images**

149 This study used two sets of SAR data (Table 1). The L-band ALOS-1 PALSAR-1 data
150 included 26 ascending images taken between December 2006 and January 2011. The
151 descending PALSAR-1 data over the study area was limited and not adopted in this study.
152 Therefore, we analyzed the LOS velocities based on these ascending PALSAR-1 images. The
153 PALSAR-1 raw data were provided by Japan Aerospace Exploration Agency (JAXA). The
154 C-band Sentinel-1 SAR data included 252 ascending and descending images between April
155 2016 and September 2021. Combining ascending and descending Sentinel-1 images allowed
156 for calculating both vertical and east-west horizontal components of LOS velocities under the
157 assumption of zero north-south components (Eq. (1-5)). Most SAR satellites, such as ALOS
158 and Sentinel-1, operate in a sun-synchronous orbit with an inclination of around 98°, resulting
159 in range observations almost in the east-west direction and rarely in the north-south direction.
160 Consequently, the north-south components cannot be extracted adequately from these SAR
161 data-derived LOS velocities (Wright et al. 2004). Using Sentinel-1 images till 2021 other than
162 till 2018 (the same end year with airborne LiDAR data) would provide a more comprehensive
163 understanding of the subsidence pattern for our study area. The Sentinel-1 single look
164 complex (SLC) data were provided by the Copernicus program of the European Space
165 Agency. Full details of the InSAR data are presented in Supplementary Information.
166

Table 1. Characteristics of SAR data.

Characteristics \ Sensor	ALOS-1 PALSAR-1	Sentinel-1
Band (Wavelength)	L (23.6 cm)	C (5.6 cm)
Beam mode	FBS, FBD	IW
Revisit time	46 days	12 days
Orbital geometry	Ascending	Ascending/Descending
Path	175	136/143
Frame	570, 580	90-93/491-494
Temporal span	12/2006-1/2011	4/2016-9/2021

3.2.2 SBAS InSAR Analysis

We used the SBAS method to retrieve historical subsidence from SAR images. The SBAS method utilizes interferograms from small temporal and spatial baseline subsets, reducing both spatial and temporal decorrelation and improving phase estimates' performance (Berardino et al. 2002). Persistent Scatterer Interferometry (PSI) uses persistent scatterers (PS) to obtain the land surface displacements (Ferretti et al. 2001). The persistent scatterers are always substantial in developed urban areas, which renders PSI to be applied more in the urban area. In this study, the study area covers developed urban areas, grassland areas, and wetlands. One of our objectives is investigating the relationship between land subsidence and land cover. SBAS method can overcome the rapid loss of coherence in long-term interferograms in PSI over nonurban areas. So, although PSI can achieve full-resolution (single-look), this study finally applied the SBAS method to map the land subsidence.

For the ALOS-1 PALSAR-1 data, we selected the image collected on 28 March 2008 as the reference image. All other images were coregistered to this reference image. The temporal and perpendicular baseline thresholds for PALSAR-1 data were set as 1,200 days and 1,500 m, respectively (Fig. 3a). For the Sentinel-1 data, the image collected on 10 January 2019 was chosen as the reference image. Interferograms were generated between each epoch and the adjacent four epochs for Sentinel-1 data (Fig. 3b and 3c). This study used the InSAR Scientific Computing Environment (ISCE) (Rosen et al. 2012) to obtain 49 and 1012 interferograms for PALSAR-1 and Sentinel-1 stacks, respectively. The multilooking approach was leveraged to alleviate the phase noise, which was 9×2 (azimuth by range) and 2×10 for the PALSAR-1 and Sentinel-1 data, respectively, leading to approximately 30-m pixels. The topographic phase was removed from interferograms based on a 30-m Shuttle Radar Topography Mission DEM. In addition, orbit parameters were incorporated to correct orbital errors in the generation of Sentinel-1 interferograms. All interferograms were unwrapped by adopting the SNAPHU (Statistical-Cost Network-Flow Algorithm for Phase Unwrapping) (Chen and Zebker 2002).

The Miami InSAR time-series software in Python (MintPy) (Yunjun et al. 2019) was applied to perform the SBAS approach. This study selected the interferogram network by utilizing minimum spanning tree (MST) and spatial coherence threshold, i.e., accomplished the MST first by using the inverse of average spatial coherence of all interferograms as weight, then excluded the interferograms (except for MST's interferograms) with spatial coherence lower than the threshold. Average spatial coherence thresholds of 0.6 for the Sentinel-1 interferograms and 0.65 for PALSAR-1 interferograms were applied in this study (Fig. 3). For

the Sentinel-1 interferogram network, the temporal baseline threshold of not exceeding 100 days was applied then (Fig. 3b and 3c). Water bodies were masked out by applying a DEM-based water mask in radar coordinates. We selected two buildings as reference points for PALSAR-1 and Sentinel-1 datasets (magenta dots, denoted as Ref. in Fig. 1b). All interferograms were referenced to the reference point so that the relative LOS velocities can be calculated later. The components of tropospheric delay were removed by ERA5 reanalysis using PyAPS (Python-based Atmospheric Phase Screen estimation) module (Jolivet et al. 2011). This study estimated the LOS velocity as the slope of the best fitting line to the range change time series and the uncertainty of the velocity as the goodness of fit, i.e., standard deviation (Fattahi and Amelung 2015).

The LOS velocity v_{los} can be decomposed into three velocity components in the east-west direction (v_E), the north-south direction (v_N), and the vertical direction (v_V) (Fialko and Simons 2001; Wright et al. 2004):

$$v_{los} = \begin{pmatrix} -\sin\theta\cos\alpha & \sin\theta\sin\alpha & \cos\theta \end{pmatrix} \begin{pmatrix} v_E \\ v_N \\ v_V \end{pmatrix} \quad (1)$$

where θ is the radar incidence angle and α is the satellite heading angle (i.e., the direction of the satellite motion). The incidence angle and heading angle are known. In this study, for Sentinel-1 ascending and descending geometries, the mean values for the incidence angles are 32.55° and 32.50°, and the heading angles are 349.22° and 190.79°, respectively. Based on estimated Sentinel-1 ascending LOS velocities v_{los}^{AS} and descending LOS velocities v_{los}^{DS}, Eq. (2) and Eq. (3) can be developed with three unknown velocity components v_E, v_N, and v_V:

$$v_{los}^{AS} = -\sin_{\theta}^{\mathrm{AS}}\cos_{\alpha}^{\mathrm{AS}} v_E + \sin_{\theta}^{\mathrm{AS}}\sin_{\alpha}^{\mathrm{AS}} v_N + \cos_{\theta}^{\mathrm{AS}} v_V \quad (2)$$

$$v_{los}^{DS} = -\sin_{\theta}{}^{\mathrm{S}}\cos_{\alpha}{}^{\mathrm{S}} v_E + \sin_{\theta}{}^{\mathrm{S}}\sin_{\alpha}{}^{\mathrm{S}} v_N + \cos_{\theta}{}^{\mathrm{S}} v_V \quad (3)$$

Assuming that the motion in the north-south direction (v_N) is negligible, Eq. (2) and Eq. (3) could be solved to yield the LOS velocity projections onto the vertical (v_V, Eq. (4)) and east-west horizontal direction (v_E, Eq. (5)):

$$v_V = \frac{\sin_{\theta}^{\mathrm{DS}}\cos_{\alpha}^{\mathrm{DS}}\ v_{los}^{AS} - \sin_{\theta}^{\mathrm{AS}}\cos_{\alpha}^{\mathrm{AS}} v_{los}^{DS}}{\cos_{\theta}^{\mathrm{AS}}\sin_{\theta}^{\mathrm{DS}}\cos_{\alpha}^{\mathrm{DS}} - \sin_{\theta}^{\mathrm{AS}}\cos_{\alpha}^{\mathrm{AS}}\cos_{\theta}^{\mathrm{DS}}} \quad (4)$$

$$v_E = \frac{\cos_{\theta}^{\mathrm{AS}} v_{los}^{DS} - \cos_{\theta}^{\mathrm{DS}} v_{los}^{AS}}{\sin_{\theta}^{\mathrm{AS}}\cos_{\alpha}^{\mathrm{AS}}\cos_{\theta}^{\mathrm{DS}} - \cos_{\theta}^{\mathrm{AS}}\sin_{\theta}^{\mathrm{DS}}\cos_{\alpha}^{\mathrm{DS}}} \quad (5)$$

During the data processing, by inputting Sentinel-1 ascending and descending geometries LOS velocities in the decomposition operation of MintPy, the Sentinel-1 vertical components under the assumption of zero north-south motion will be generated. For the PALSAR-1 ascending geometry used in this study, only Eq. (2) could be developed. With three unknown velocity components, the study estimated the vertical components of PALSAR-1 LOS velocities using Eq. (6). This equation was derived from Eq. (2) by assuming that the east-west and north-south motion were negligible. The mean incidence angle for PALSAR-1 data is 39.7°. This decomposition was executed in the calculation operation of MintPy.

$$v_V = \frac{v_{los}^{AS}}{\cos_{\theta}^{\mathrm{AS}}} \quad (6)$$

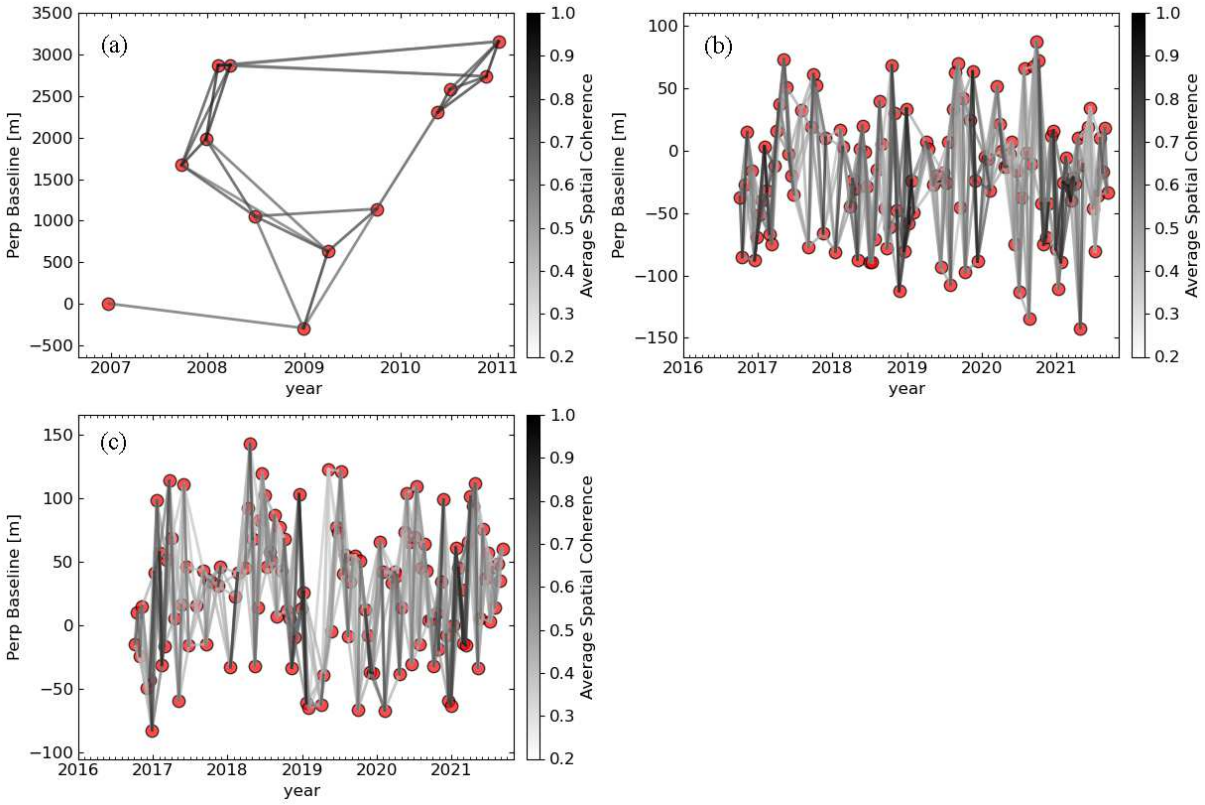

Figure 3. Interferogram networks from ALOS-1 PALSAR-1 and Sentinel-1 acquisitions with perpendicular and temporal baselines: (a) PALSAR-1 ascending images, (b) Sentinel-1 ascending images, and (c) Sentinel-1 descending images. Red circles represent SAR images.

3.2.3 Validation Based on GPS Data

A CORS GPS station (TXLM) is located in a highly developed area of the study site (Fig. 1b). The GPS data for 2006-2021 were provided by the National Geodetic Survey (NGS) and processed by the Nevada Geodetic Laboratory with respect to the IGS14 reference frame (Blewitt et al. 2018). We used the GPS vertical land surface displacement measurements to validate our InSAR-based subsidence results over an approximately 30 m × 30 m area centered on the GPS station.

250

251 **3.3 Airborne LiDAR-Based Land Surface Difference**

252 We used two airborne LiDAR point cloud datasets of 2006 and 2018, provided by the 3D
253 Elevation Program (3DEP) of the United States Geological Survey (USGS). These datasets'
254 vertical and horizontal datums were NAVD88 and NAD83, respectively. The point density of
255 the 2006 data was below 2 points/m^2 and was deemed adequate to generate a 1-m DEM. 14
256 categories were classified for the LAS airborne LiDAR point cloud data according to the
257 ASPRS classification standard. This study leveraged the ground class of the point cloud and
258 applied a standard filtering procedure to extract the bare earth point cloud data (Fig. 2). DEM
259 tiles were generated based on those ground points using the LAStools and were merged then
260 to produce a seamless 1-m DEM. For the 2018 DEM, raw 1-m DEM tiles (1.65 km × 1.85 km)
261 were downloaded from 3DEP and merged into a DEM using QGIS. The airborne LiDAR data
262 in 2018 was offered at level 2 (QL2), which had a minimum nominal pulse spacing (NPS) of
263 0.7 m and a vertical error of 0.1 m, measured as root mean square error (RMSE). Finally, the
264 land surface differences in the vertical direction between 2006 and 2018 were calculated
265 based on two temporal DEMs using subtraction analysis in QGIS (Fig. 2). The uncertainties
266 of surface differences were unlikely to be spatially homogeneous, caused by factors such as
267 uncertainties of original DEMs and the error propagation during the change detection. The
268 uncertainties of airborne LiDAR-derived DEM were also heterogeneous but always offered as
269 a single value. In this study, the absolute vertical accuracy for QL2 airborne LiDAR data was

provided in the USGS report as 0.1 m, but the relative vertical accuracy would be smaller than 0.06 m for smooth surfaces. Quantifying uncertainty in change detection results of airborne LiDAR is not a trivial work and is still very limited (Okyay et al. 2019). Land surface difference from airborne LiDAR includes the accumulation of gradual land subsidence and land displacements induced by human activities and other surface processes. The periods of airborne LiDAR measurements (2006-2018) had overlaps with that of ALOS-1 PALSAR-1(2006-2011) and Sentinel-1(2016-2021) SAR data. This study compared airborne LiDAR-derived land surface differences to the InSAR-derived velocities. The 1-m map of land surface differences would complement the PALSAR-1 and Sentinel-1 results by revealing more details of the spatial variations of gradual subsidence below the scale of the 30-m InSAR pixels and identifying the significant land surface change which InSAR cannot capture.

3.4 Subsidence Analysis over Different Coastal Land Cover and Topographic Patterns

We obtained the 30-m 2019 land cover from the National Land Cover Database (NLCD). USGS generated the NLCD products through integrating multi-source geospatial datasets and classification using machine learning methods (Jin et al. 2019), and their accuracies were validated at the national level (Wickham et al. 2021).

The land cover analysis was conducted in ArcGIS Pro. First, the NLCD data was extracted and clipped to the same extent as the study area. Then, the NLCD categories were

290 modified to address the land cover pattern of the study area. Deciduous forest, evergreen
291 forest, and mixed forest categories were merged into a forest category. Shrub/scrub,
292 grassland/herbaceous, pasture/hay, and cultivated crops categories were merged into a
293 grassland category. Woody wetlands and emergent herbaceous wetlands categories were
294 merged into a wetlands category. The resulted land cover raster was converted into
295 multi-feature polygons. These polygons were linked to the subsidence estimates using the
296 Spatial Join Tool in ArcGIS Pro. Based on attribute tables of the Spatial Join-derived feature
297 classes, mean subsidence velocities, standard error, and interquartile ranges were calculated
298 for different land cover categories. In addition, linear regression was performed to analyze the
299 relationship between subsidence velocities and surface imperviousness at the pixel level and
300 between mean subsidence velocities and surface imperviousness at the class level.

301 We further examined the relationship between subsidence and topography using the
302 2018 airborne LiDAR DEM. The floating-type DEM was first converted into an integer-type
303 DEM and then into polygon features. Next, we established two transect lines (Fig. 15a) to
304 represent the dominant elevation gradients over the study area, e.g., transect QI across the
305 northeast-southwest gradient from the shoreline to a river mouth and transect ST located
306 along the northwest-southeast shoreline. Then, this study applied the Stack Profile Tool in
307 ArcGIS Pro to extract elevation and subsidence velocities along these transect lines for profile
308 analysis.

309

4. Results

4.1 InSAR-Derived Subsidence Velocity

4.1.1 Spatiotemporal Pattern of Land Subsidence

The LOS velocities from ALOS-1 PALSAR-1 and Sentinel-1 images are shown in Fig. 4. Positive values indicate ground motions toward the satellite (i.e., uplift) and negative values indicate ground motions away from the satellite (i.e., subsidence). For PALSAR-1 analysis between 2006 and 2011, the LOS velocities varied from −33 to 20 mm/year (Fig. 4a) with the standard deviations of 0 to 12 mm/year (Fig. 4b). Results show that the significant subsidence in 2006-2011 tended to continue in the next time window analyzed and with a similar magnitude. From 2016 to 2021, the LOS velocities ranged from −31 to 19 mm/year for Sentinel-1 ascending geometries analysis (Fig. 4c) and ranged from −31 to 17 mm/year for descending geometries analysis (Fig. 4e). The standard deviations of LOS velocities for Sentinel-1 ascending and descending geometries were smaller than 2 mm/year (Fig. 4d and 4f).

The velocities in the vertical direction under the assumption of zero north-south motion in 2016-2021 based on both ascending and descending Sentinel-1 images are shown in Fig. 5. For velocities in the vertical direction, positive and negative values indicate ground uplift and subsidence, respectively. This study found that the vertical velocities were up to −34 mm/year, with a spatial pattern similar to that of the LOS velocities (Fig. 4c and 4e). Our findings agreed with the results from a previous InSAR study in this region (Miller and Shirzaei

330 2021).

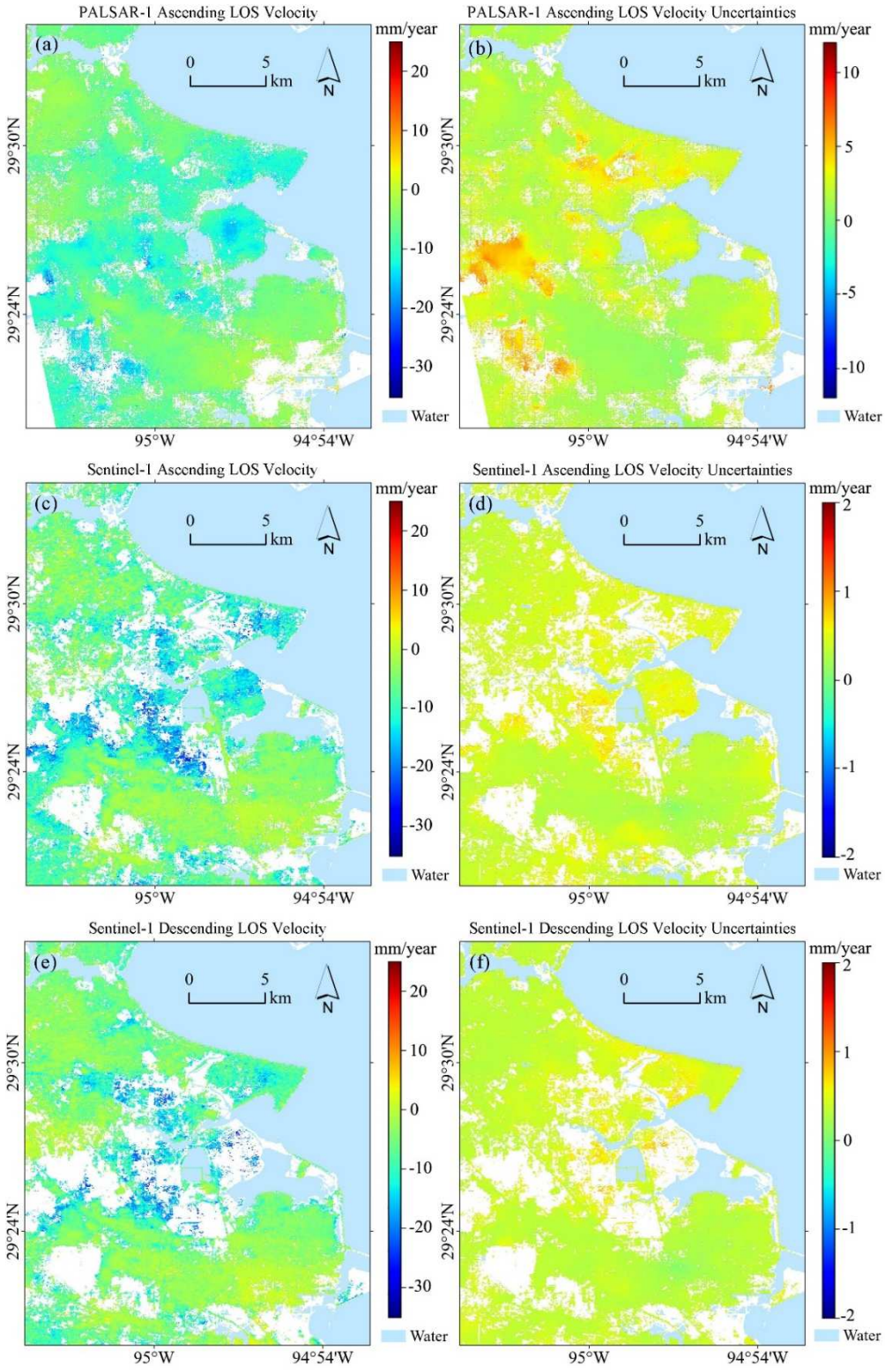

331

332 **Figure 4**. LOS velocities and standard deviations derived from (a and b) PALSAR-1

ascending images (2006-2011), (c and d) Sentinel-1 Path 136 ascending images (2016-2021), and (e and f) Sentinel-1 Path 143 descending images (2016-2021).

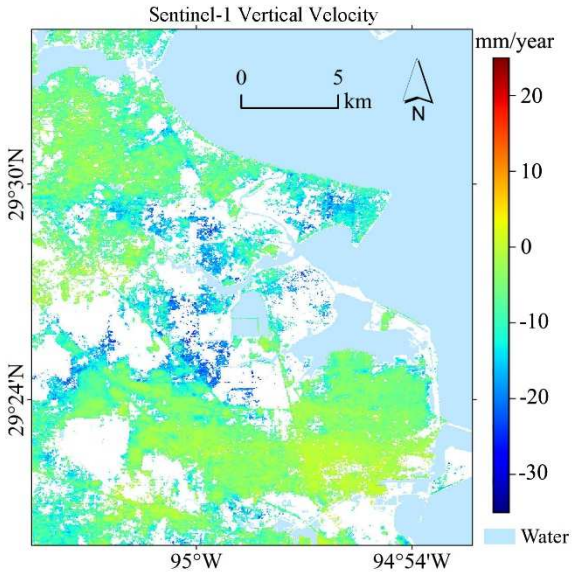

Figure 5. The vertical components under the assumption of zero north-south motion in 2016-2021 based on Sentinel-1 ascending and descending LOS results (Fig. 4c and 4e).

4.1.2 Validation

Fig. 6 shows the validation of subsidence velocities in the vertical direction against the vertical GPS measurements, all presented in the form of accumulative depth. For the ALOS-1 PALSAR-1 results, only ascending data were available over the study area. Therefore, the vertical velocities transformed from LOS velocities using the local incidence angle were used for validation, assuming that the vertical component dominated the subsidence. For the Sentinel-1 results, the derived vertical velocities under the assumption of zero north-south motion (Wright et al. 2004) were directly compared to vertical GPS measurements. The GPS

measurements agreed well with both PALSAR-1 results from 2006 to 2011 (RMSE = 7.5 mm) and Sentinel-1 results from 2016 to 2021 (RMSE =11.6 mm).

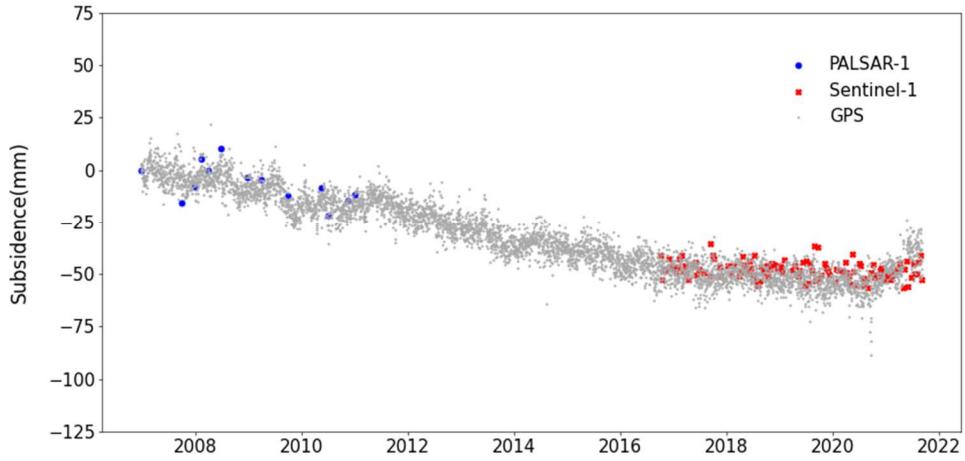

Figure 6. Comparison of InSAR-derived cumulative subsidence to GPS measurements in the vertical direction. The location of the TXLM GPS station is shown in Figure 1.

4.2 Airborne LiDAR-Derived Land Surface Difference

Here we compare the results of InSAR and airborne LiDAR over a subset of the study area that experienced substantial subsidence (Fig. 7, also marked as a blue rectangle in Fig. 1b). InSAR results (Fig. 7c and 7d) included some empty pixels because of the temporal coherence thresholds setting used to ensure reliable estimates. In contrast, the 1-m ground differences between 2006 and 2018 based on two temporal airborne LiDAR data covered the entire area (Fig. 7b). As the airborne LiDAR measurements were in the vertical direction, LOS PALSAR-1 results-derived vertical components based on Eq. (6) (Fig. 7c) and Sentinel-1 vertical results (Fig. 7d) were used here. The PALSAR-1 results indicated a strong

362 subsidence process (up to −22 mm/year) in 2006-2011 (Fig. 7c). The subsidence process
363 appeared to be continuing at several locations in 2016-2021 from Sentinel-1 results (Fig. 7d),
364 and the subsidence velocities in the vertical direction were up to −25 mm/year. In the
365 upper-right part, the vertical velocities derived from PALSAR-1 images under the assumption
366 of no east-west and north-south motion (Fig. 7c) were larger than that from Sentinel-1 images
367 under the assumption of no north-south motion (Fig. 7d). Groundwater use, human activities
368 such as building construction, etc. might lead to quicker subsidence in 2006-2011 than in
369 2016-2021. In the selected area, airborne LiDAR results revealed plenty of areas with a
370 surface change between −0.3 to 0.1 m (Fig. 7b). Limited and scattered areas were with large
371 surface changes (negative or positive), which were likely induced by human activities and
372 other surface processes (for example, areas A1 and A2 highlighted in Fig. 7a). Overall, both
373 InSAR-based analysis and airborne LiDAR measurements indicated substantial subsidence in
374 this area. Most highly subsided areas based on InSAR analysis also showed relatively large
375 surface changes based on airborne LiDAR measurements, between −0.1 to −0.3 m during
376 2006-2018 (Fig. 7). The 1-m airborne LiDAR results offered more details of the surface
377 differences and could capture some large changes that InSAR cannot monitor.

378 We further conducted profile analysis along two transect lines (Fig. 7a) to evaluate the
379 agreement and disagreement between InSAR and airborne LiDAR estimates. The transect line
380 L1 represented the northwest-southeast direction, with the land use dominated by developed
381 and vegetated areas. PALSAR-1 and Sentinel-1 results presented a trend similar to that of the
382 accumulative land surface differences in 2006-2018 from the airborne LiDAR results (Fig. 8a

383 and 8b). The lower subsidence velocities tended to be associated with smaller accumulative
384 surface differences, and higher velocities aligned with greater accumulative surface
385 differences. In particular, the airborne LiDAR results of sections BC and DE exhibited large
386 land surface differences. The PALSAR-1 and Sentinel-1 velocities showed high values in
387 these sections, especially velocities from Sentinel-1 analysis (up to about −20 mm/year). The
388 high velocities would contribute to the large subsidence, which had a good agreement with
389 the airborne LiDAR results (Fig. 8b). Based on Google historical images, section BC was on a
390 piece of land with some grass and almost had no change from 2006 to 2011 (Fig. 9a). This
391 area was influenced by a pool and other activities then, confirming the great variations of
392 Sentinel-1 subsidence velocities (Fig. 8b). Section AB subsided from both PALSAR-1 and
393 Sentinel-1 results, whereas airborne LiDAR results presented some uplift. Based on this
394 multi-period information, we could infer that this segment had an uplift in 2011- 2016.

395 The transect line L2 represented the southwest-northeast direction. Sentinel-1 velocities
396 trend almost fits well with the land surface difference trend as shown in airborne LiDAR
397 results (Fig. 8d). PALSAR-1 velocities trend of the sections starting around H fits relatively
398 well with the land surface difference trend (Fig. 8c). Sentinel-1 analysis showed high
399 velocities in the vertical direction over the area where airborne LiDAR obtained large surface
400 differences. In particular, sections GH and IJ underwent larger subsidence in 2016-2021 than
401 in 2006-2011, leading to some large subsidence in agreement with airborne LiDAR results
402 (Fig. 8c and 8d). The airborne LiDAR results show a heterogeneous pattern of surface change
403 along section HI, agreed better with Sentinel-1 results than PALSAR-1 results. As shown in

Fig. 9b, the area along the HI was mainly dominated by grassland in 2006-2011 and had a relatively homogeneous subsidence pattern accordingly (Fig. 8c). Within the period of Sentinel-1 results (2016-2019), the area along the HI was disturbed and/or changed by some land reclamation and construction activities (Fig. 9b), leading to a heterogeneous subsidence trend as well as some substantial surface changes that could only be captured by airborne LiDAR (Fig. 8d). Sections FG subsided much faster in 2006-2011 than in 2016-2021, and the land surface change was relatively small. Overall, the land surface difference pattern derived from airborne LiDAR data between 2006 and 2018 generally agreed with InSAR-derived velocities along the selected transect lines and provided a more effective means to characterize large surface changes in areas with human activities.

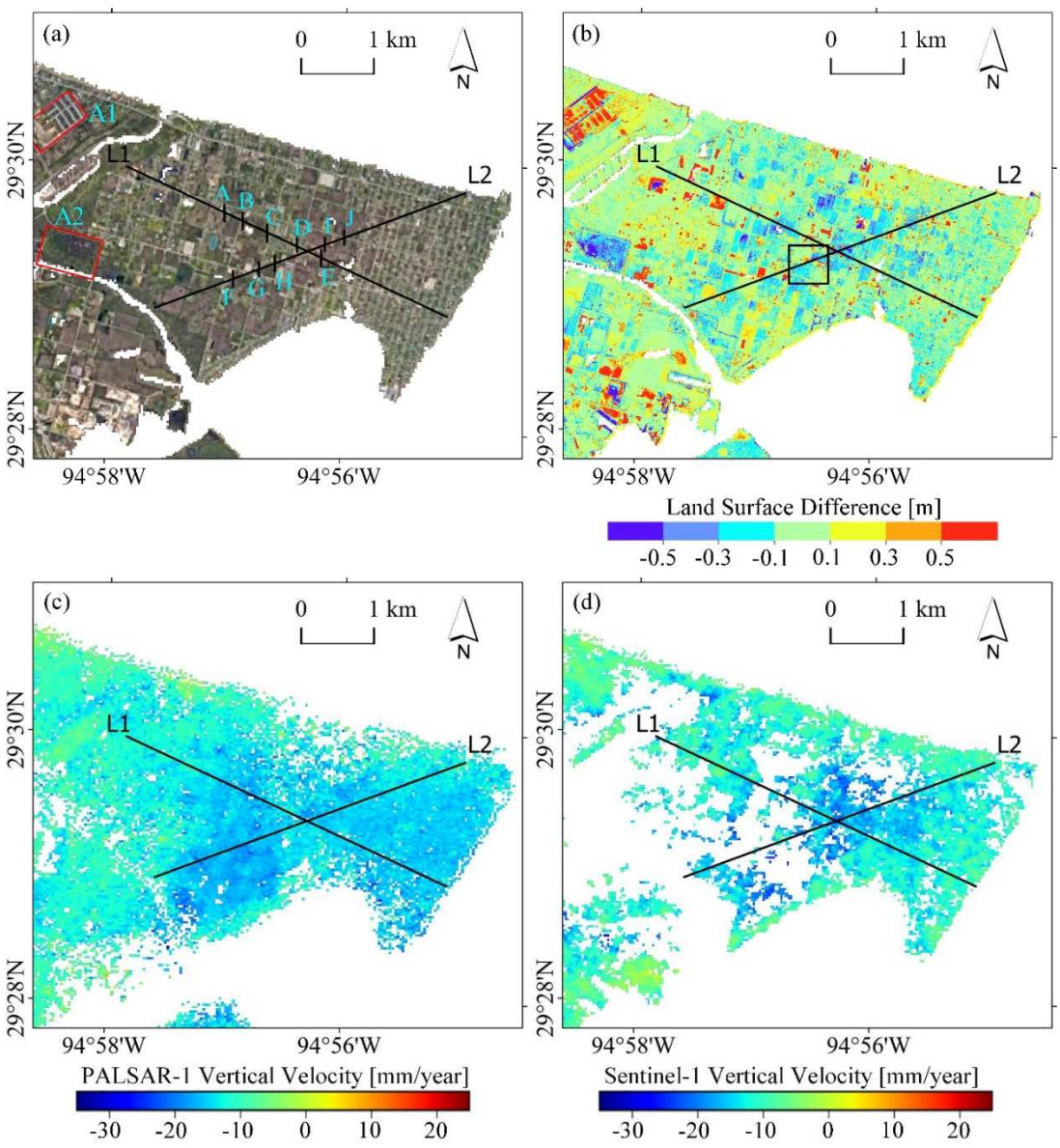

414

415 **Figure 7**. Detailed subsidence pattern of a selected area: (a) Google Earth image, (b) airborne

416 LiDAR-derived vertical surface differences, (c) vertical component based on PALSAR-1

417 results (assuming no east-west and north-south motions), and (d) vertical component based on

418 Sentinel-1 results (assuming no north-south motion). Figure 1b shows the location of this

419 area.

420

421

422

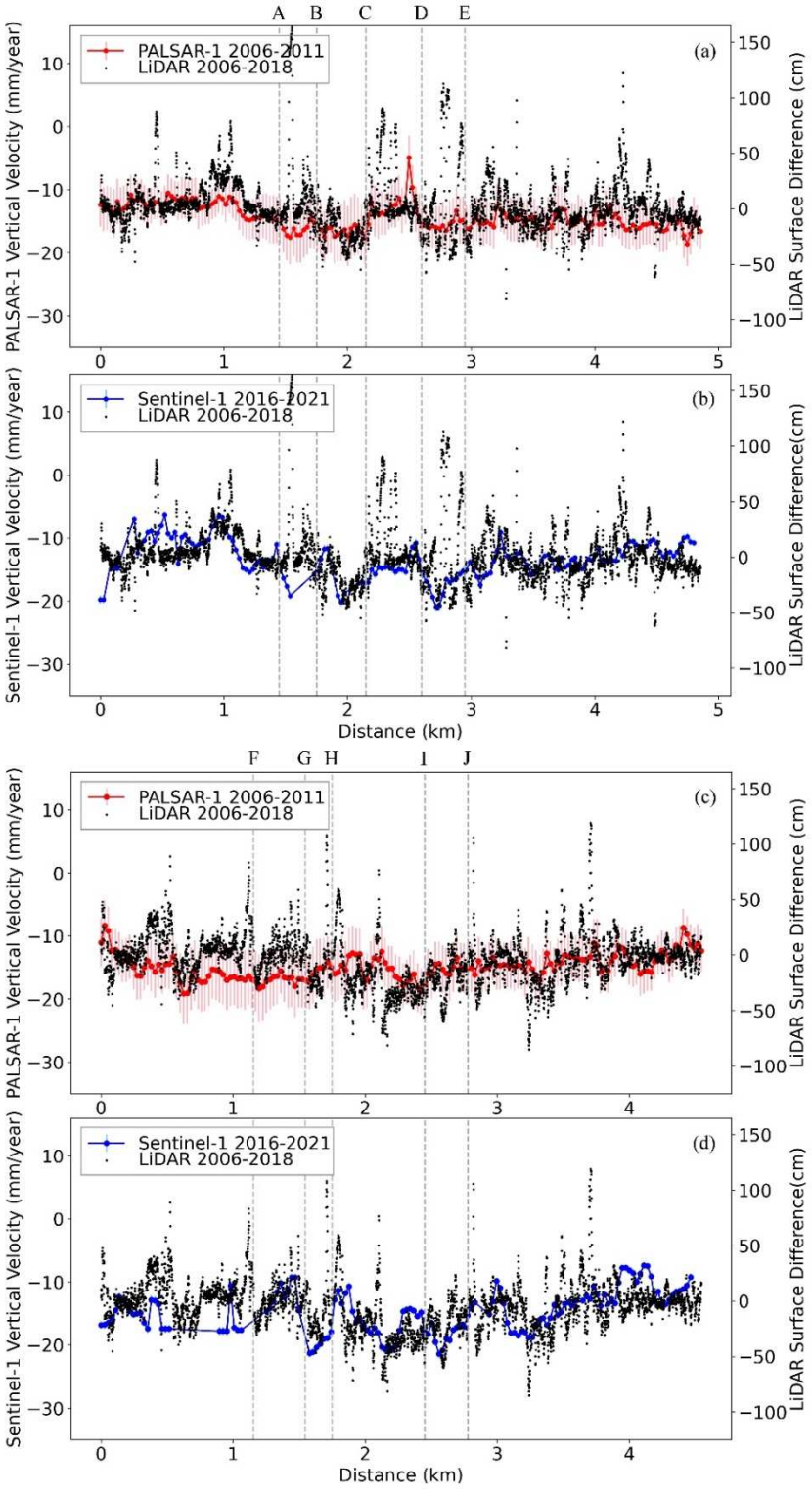
A
B
C
D
E
PALSAR-1 2006-2011
LiDAR 2006-2018
(a)
PALSAR-1 Vertical Velocity (mm/year)
LiDAR Surface Difference (cm)
Sentinel-1 2016-2021
LiDAR 2006-2018
(b)
Sentinel-1 Vertical Velocity (mm/year)
LiDAR Surface Difference(cm)
Distance (km)
F
G
H
I
J
PALSAR-1 2006-2011
LiDAR 2006-2018
(c)
PALSAR-1 Vertical Velocity (mm/year)
LiDAR Surface Difference (cm)
Sentinel-1 2016-2021
LiDAR 2006-2018
(d)
Sentinel-1 Vertical Velocity (mm/year)
LiDAR Surface Difference(cm)
Distance (km)

423

Figure 8. Comparison of InSAR and airborne LiDAR results along transect lines L1 (a and b) and L2 (c and d). Error bars indicate standard deviations. The locations of the transect lines are shown in Figure 7a.

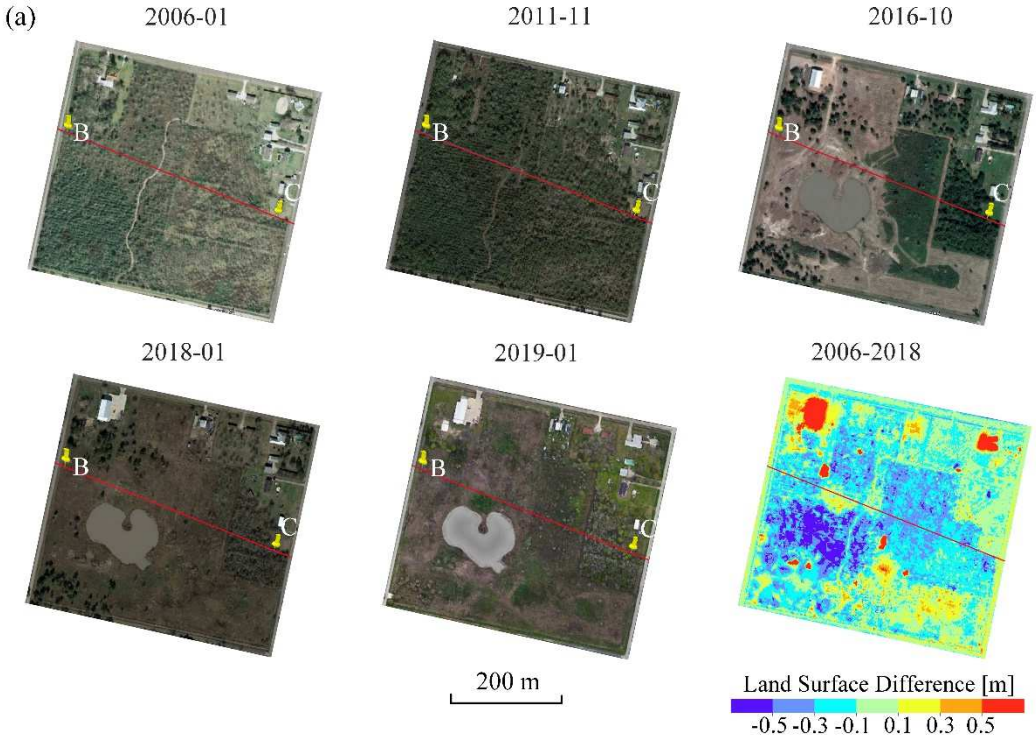

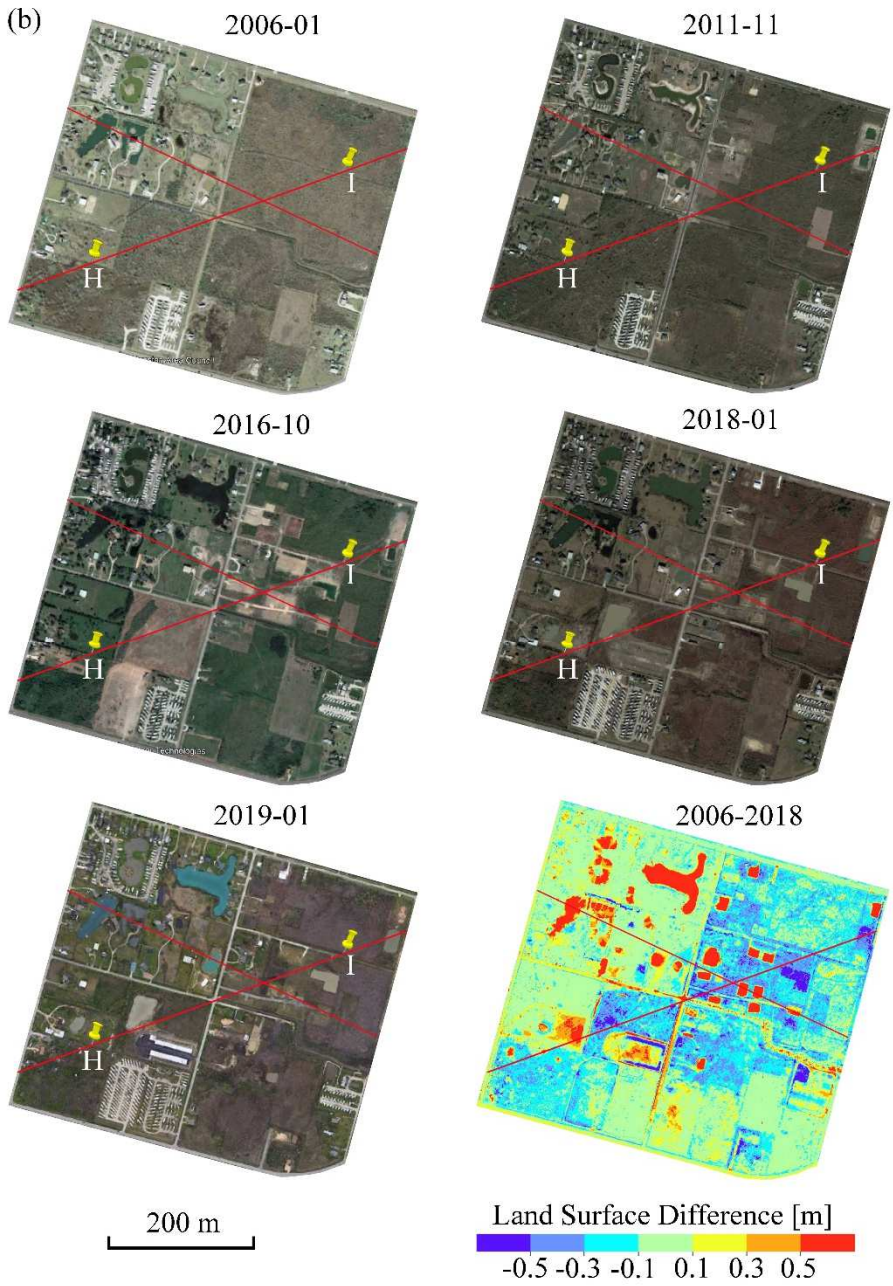

428

429 **Figure 9.** Historical Google Earth images and airborne LiDAR-derived land surface

430 differences over the selected profiles BC (a) and HI (b). The locations of BC and HI are

431 shown in Fig. 7a.

432 Checkpoints B, C, H, and I are denoted by yellow placemarks.

4.3 Relationships between Subsidence and Land Cover

Based on the land cover pattern of the study area, the standard NLCD land cover categories were re-classified as developed building area, barren land, forest area, grassland area, wetland area, and open water (Fig. 10). Developed areas included four classes based on percent impervious surface coverage: open space area (1%-20%), low-intensity area (20%-49%), medium intensity area (50-79%), and high-intensity area (80%-100%). This study analyzed the subsidence (Fig.4a and Fig.5) distribution for different land cover types (Fig. 10) over the entire study area. Results showed relatively high subsidence velocities in grassland, forest, wetlands, and barren land (Fig. 11). By contrast, the classes of developed areas had relatively low subsidence velocities. In particular, the developed high-intensity area was associated with the lowest subsidence velocities among all categories (Fig. 11). The velocities based on Sentinel-1 analysis were more dispersed than that from PALSAR-1 analysis for each land type (Fig. 11c and 11d).

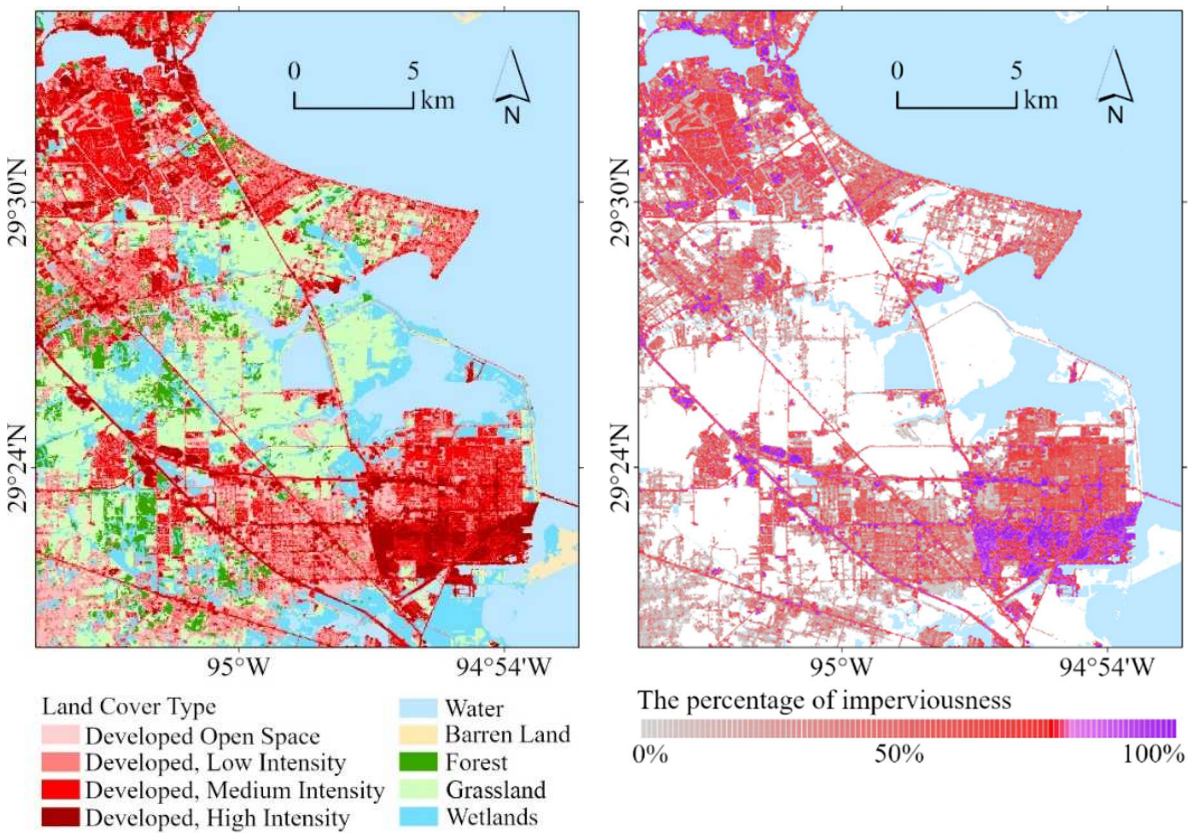

447

448 **Figure 10**. Land cover of the study area based on NLCD 2019.

449

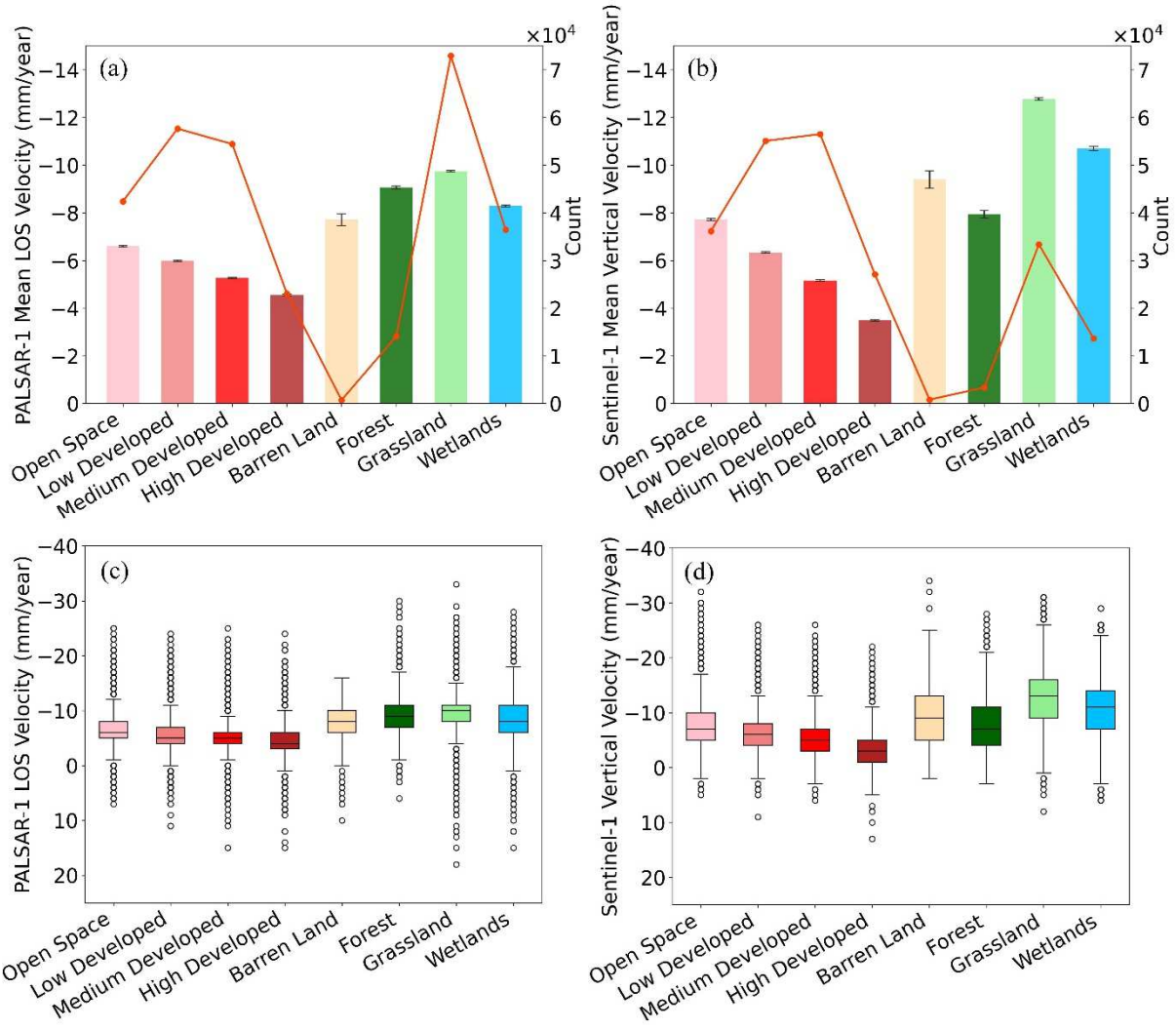

Figure 11. PALSAR-1 mean LOS velocities (a) and Sentinel-1 mean vertical velocities (b) for different land cover types. The 95% confidence intervals are computed as 1.96 standard errors for each land type. The red line represents the number of pixels. Subplots c and d show the interquartile ranges of PALSAR-1 LOS velocities and Sentinel-1 vertical velocities for different land cover types, respectively.

This study then used linear regression to explore the relationship between the percent surface imperviousness (Fig. 10) and subsidence velocities (Fig. 4a and Fig. 5) at two

459 different scales (Fig. 12) over the entire study area. First, for all individual 30-m pixels, the
460 least squares polynomial fit (first degree) was applied to model the relationship between the
461 percent surface imperviousness and subsidence velocities (Fig. 12a and 12c). Results indicate
462 that surface imperviousness was negatively correlated with the magnitude of subsidence
463 velocities derived from both PALSAR-1 images (R^2 = 0.207) and Sentinel-1 images (R^2 =
464 0.265). Second, 30-m pixels with the same percent imperviousness value were extracted and
465 clustered in 1% intervals from 0% to 100%, resulting in 100 clusters in which each cluster
466 with the same imperviousness value included many pixels with various subsidence velocities.
467 This study calculated the mean subsidence velocities for the resulted 100 clusters. Then, for
468 the clustering results, the least squares polynomial fit (first degree) was used again to model
469 the relationship between the percent surface imperviousness and the mean subsidence
470 velocities (Fig. 12b and 12d). Results showed that the clustering procedure led to higher
471 correlations between surface imperviousness and subsidence velocities for both PALSAR-1
472 (R^2 = 0.895) and Sentinel-1 (R^2 = 0.937).

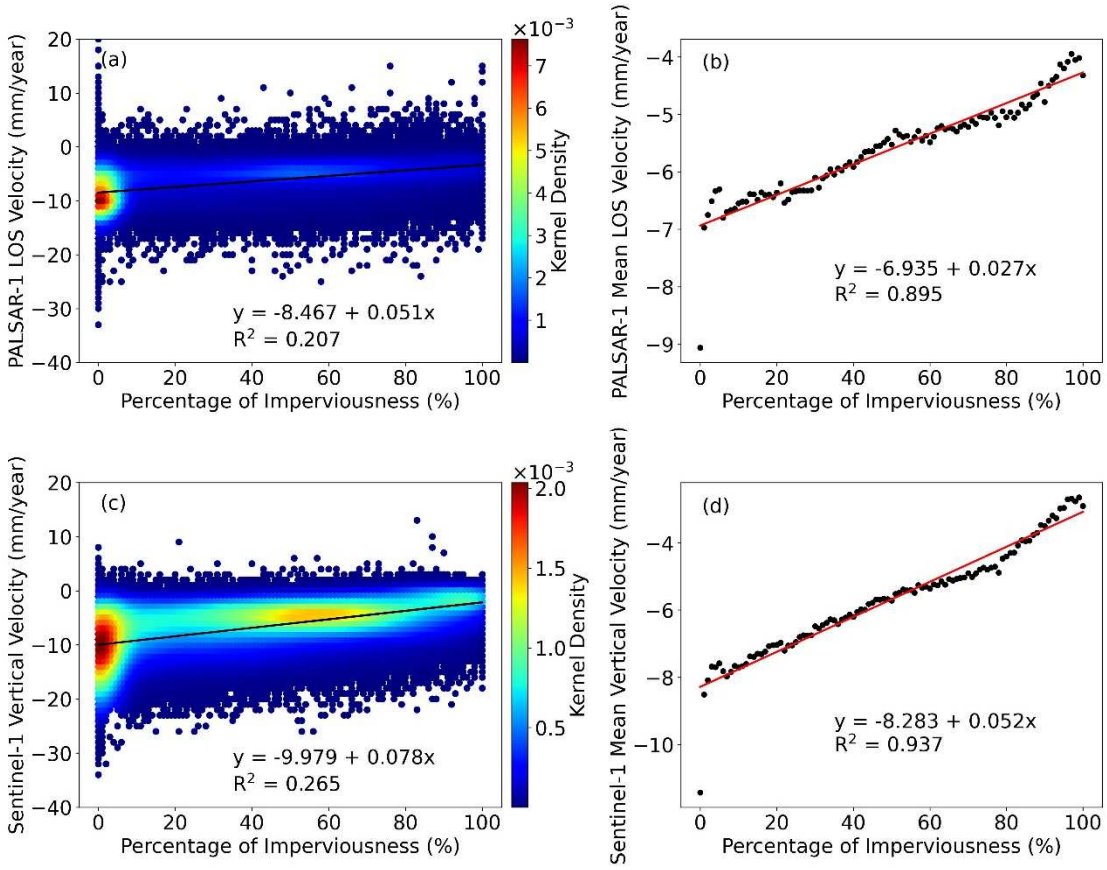

Figure 12. Relationships between percent impervious coverage and subsidence velocities: PALSAR-1 LOS velocities at (a) the pixel level and (b) the cluster level; Sentinel-1 vertical velocities at (c) the pixel level and (d) the cluster level. Black lines (a and c) and red lines (b and d) indicate linear fit.

5. Discussion

5.1 Improvements in Existing Coastal Subsidence Investigation

Coastal subsidence studies often have high expectations of spatial resolution and vertical accuracy to meet the requirements of various coastal studies such as flood risk analysis, shoreline erosion control, etc. InSAR works well in monitoring the gradual land subsidence

484 with high accuracy over the coastal areas (Higgins et al. 2014). However, it cannot capture
485 significant surface displacements in a short time due to decorrelation. On the other hand,
486 airborne LiDAR can monitor the land surface difference with a high spatial resolution (Jones
487 et al. 2013). In this study, airborne LiDAR datasets contributed to a 1-m land surface
488 difference mapping with about 10 cm vertical accuracy. Land surface change includes the
489 accumulation of gradual land subsidence and land displacements induced by human activities
490 and other surface processes. The results of this study indicate the unique benefits of
491 combining InSAR and airborne LiDAR measurements to improve the understanding of the
492 spatiotemporal pattern of subsidence.

493 From the spatial perspective, InSAR analysis based on PALSAR-1 and Sentinel-1
494 images was constrained by its relatively low spatial resolution. However, the detailed surface
495 changes derived from the 1-m airborne LiDAR results can contribute to a better
496 understanding of the spatial variability of land deformation within the 30-m InSAR pixel. As
497 demonstrated in the first example in Fig. 13, the gradual subsidence over a piece of land with
498 some grasses was consistently captured in both InSAR and airborne LiDAR results (Fig. 13a).
499 PALSAR-1 and Sentinel-1 results indicated moderate subsidence rates of −0.9 to −1.5
500 cm/year, while airborne LiDAR results also suggested a moderate magnitude of the total
501 surface change between −0.1 to −0.3 m over 12 years. In addition to the consistent
502 characterization of an overall moderate subsidence process, the airborne LiDAR result
503 revealed a higher degree of spatial heterogeneity. Besides, for areas with significant surface
504 displacements over a short time which InSAR cannot capture, the additional surface change

505 information from airborne LiDAR could contribute to the analysis at the block or even
506 building scale, playing a critical role in high-resolution hydraulic and hydrologic simulations
507 in coastal regions. These relatively large surface displacements occure most likely due to
508 human activities changing the structure of the upper ground such as modifications related to
509 roads and drainage structures construction or building foundations. The second example (Fig.
510 13b) illustrated a large surface deformation caused by the construction of a stormwater
511 drainage system for a new RV parking lot. It involved some local elevation decreases due to
512 the elevation excavation of a stormwater ditch and some local elevation increases caused by
513 the placement of a culvert (Fig. 13b). These changes were clearly delineated in the airborne
514 LiDAR results and obviously not associated with gradual subsidence, and they were not
515 identifiable in the InSAR results. Overall, without the complementary high-resolution
516 information from airborne LiDAR results, PALSAR-1 and Sentinel-1 analysis excluded
517 important surface changes within a coarse InSAR pixel could not address significant land
518 deformation over the small dimensions of natural and built features in a heterogeneous urban
519 environment.

520 From the temporal perspective, subsidence velocities derived from PALSAR-1 and
521 Sentinel-1 images in non-overlapping periods validated and complemented the land surface
522 differences revealed by airborne LiDAR results and vice versa. In this study, InSAR analysis
523 provided subsidence velocities in 2006-2011 (PALSAR-1, Fig. 7c) and 2016-2021 (Sentinel-1,
524 Fig. 7d). Airborne LiDAR-derived land surface change estimated the total surface change
525 between 2006 and 2018 (Fig. 7b). Our analysis showed that InSAR results and airborne

LiDAR measurements fit relatively well along the selected profiles (Fig. 8). It implies that we can deduce a large land surface difference based on high PALSAR-1 and/or Sentinel-1 subsidence velocities as well as deduce high subsidence velocities from the large land surface change. The validation between high subsidence velocities and large land surface differences could be achieved. Besides, two temporal InSAR results complement the airborne LiDAR results by offering the velocities variation in the different periods. The analysis across the partially overlapping monitoring periods of airborne LiDAR, PALSAR-1, and Sentinel-1 allowed for the investigation of possible changes that took place within 2011-2016, i.e., the gap between the ALOS-1 and Sentinel-1 results. For example, the subsidence velocities of section AB (Fig. 7a) exceeded −15 mm/year in 2006-2011 and 2016-2021 (Fig. 8a and 8b). However, section AB presented limited negative land surface differences from airborne LiDAR results, which may imply some uplift from 2011 to 2016. Such partially overlapping periods of InSAR and airborne LiDAR measurements would be common in many regions, given the global availability of ALOS-1 and Sentinel-1 data. As a result, the unique advantage of including airborne LiDAR measurements could be applicable to other coastal regions.

Finally, high accuracy and resolution topography information is essential for flood risk analysis, shoreline erosion control, etc. This is particularly true for coastal plains with gentle slopes. A slight variation in the subsidence rates may significantly impact the calculations of flow directions and paths in hydrological and hydraulic simulations that are based on the subsidence-corrected DEMs. For such simulations in urban watersheds along the Texas Gulf Coast, to our knowledge, DEMs with spatial resolutions from 1-m to 10-m and vertical

accuracies below 10 cm would be desired in most cases. Some present studies try to apply high-resolution airborne LiDAR topography to the hydrological model for improving urban flooding analysis and apply UAV-collected high-resolution images for shoreline detection (Trepekli et al. 2022). This study offers 1-m land surface change results and cm-level velocities, which will contribute to a much more robust analysis.

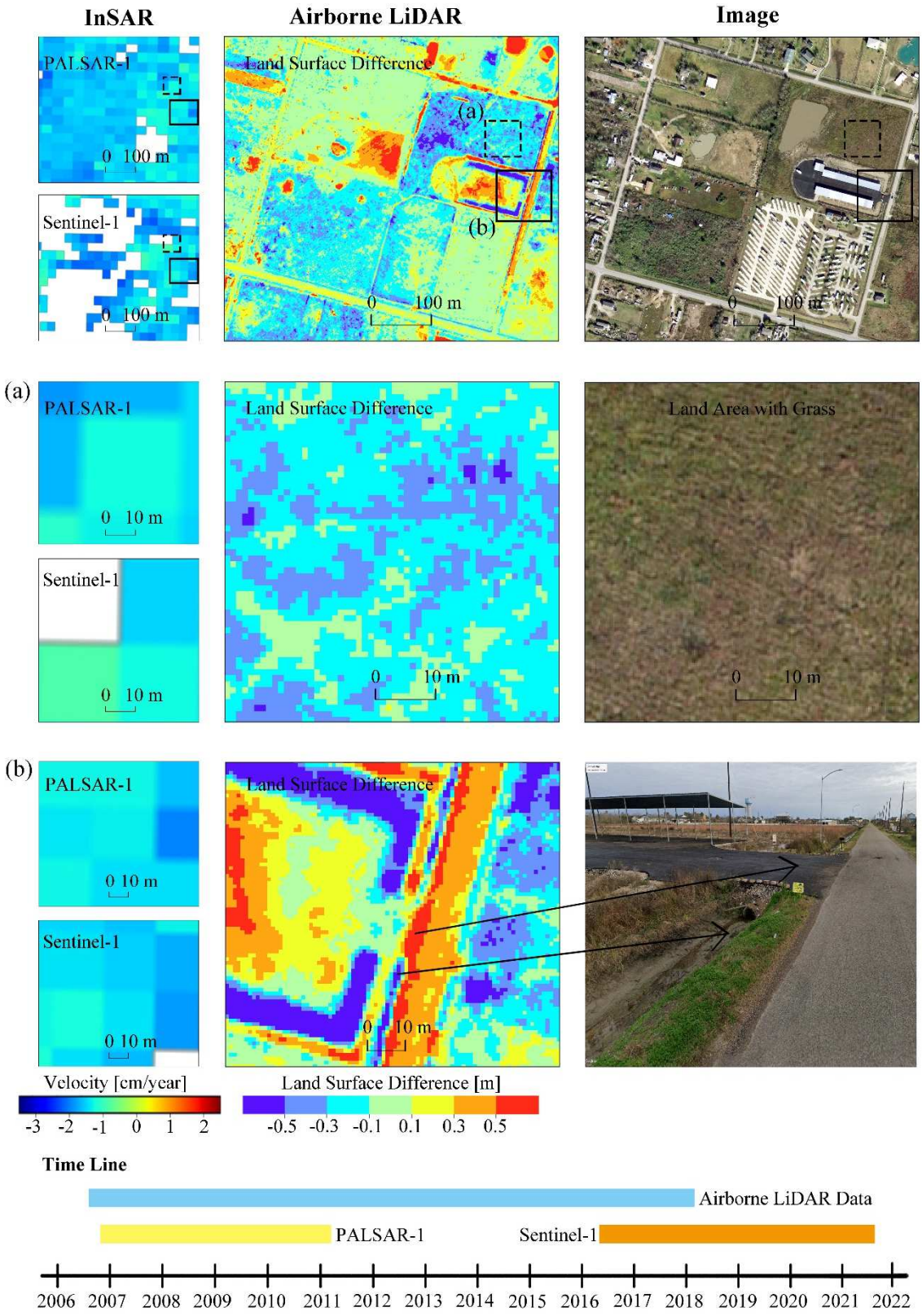

Figure 13. Examples of the multiscale measurements: (a) a grassland area (dashed box) with details presented in the second row; and (b) a developed area (solid box) with details

555 presented in the third row. In example (a), the 0.3-m HxGN aerial image shows the landscape.
556 In example (b), black arrows indicate the ditch and the culvert. This area is also marked in
557 Figure 7b.
558
559 **5.2 Limitation and Potential of Airborne LiDAR for Coastal Surface Change Mapping**
560 Point positioning accuracy of airborne LiDAR systems is influenced by system
561 calibration, time synchronization between system components, errors in the navigation
562 solution (position and attitude errors), range measurement errors, etc. (May¹ and Toth 2007),
563 which lead to a relatively low vertical accuracy (10−15 cm) of airborne LiDAR measurements.
564 The limitation of low vertical accuracy results in the fact that airborne LiDAR is a less
565 popular option for land subsidence monitoring under the conventional assumption that the
566 total subsidence will be equal to or even smaller than the errors, as well as when the
567 decision-makers are seeking very high accuracy. However, InSAR results have indicated
568 substantial subsidence rates in our study area, up to −22 mm/year in 2006-2011 (Fig. 7c) and
569 up to −25 mm/year in 2016-2021 (Fig.7d), as well as the broader Houston region, up to −30
570 mm/year in 2004-2011 (Qu et al. 2015). Given such large subsidence rates, the vertical
571 accuracy of airborne LiDAR would no longer be a constraint to decision-makers interested in
572 identifying significant surface deformation. Our results found that most highly subsided areas
573 from InSAR also showed relatively large surface changes from airborne LiDAR, between -0.1
574 m to -0.3 m during 2006-2018 (Fig. 7). The further comparison between InSAR results and

575 airborne LiDAR results along the selected profiles revealed a very similar trend in most areas
576 (Fig. 8). This proved the reliability of airborne LiDAR-derived results to some extent.
577 Furthermore, our results demonstrated that airborne LiDAR monitored the land surface
578 change from gradual land subsidence and land displacements in coastal regions. In particular,
579 land displacements caused by human activities and other surface processes tend to have
580 relatively large deformation over a short time which conventional InSAR methods cannot
581 capture.

582 While LiDAR measurements are still limited by the low vertical accuracy, few SAR
583 images could match the spatial resolution of airborne LiDAR measurements. New satellite
584 images (e.g., TerraSAR-X images) have improved spatial resolutions, but their coverage and
585 availability are far from that of Sentinel-1, resulting in relatively coarse spatial resolution of
586 InSAR analysis for lots of coastal studies. Therefore, it would be valuable to explore airborne
587 LiDAR data when these data can be readily obtained in areas that do not have high-resolution
588 SAR images yet. The spatial variability information of surface change derived from
589 multi-temporal airborne LiDAR data, even if the actual measurements are not as precise as
590 InSAR, provides invaluable higher resolution complementary information, especially for the
591 cases with large velocities that are the most important. It will benefit a variety of coastal
592 studies, particularly on the resilience of our coastal infrastructure systems, e.g., the design of
593 sea walls. This is also adaptive to flooding studies that typically require high-resolution
594 elevation information. As shown in Fig. 13b, the drainage ditch identified from the airborne
595 LiDAR results will contribute to the flooding analysis.

High-quality airborne LiDAR data spanning a long time over the coastal area is not widely distributed. Fortunately, more and more institutes, such as USGS, are opening their data nowadays. Airborne LiDAR data will be a good source of terrain information for surface change analysis over coastal areas with relatively large subsidence rates. Acting as complementary information, airborne LiDAR will be a potential opportunity for coastal studies.

5.3 Forest Influence over the InSAR Analysis

The wavelength of radar waves plays an important role in applications of InSAR over densely forested areas (Xu et al. 2021). The penetration capability of short-wavelength (3.1 cm for X-band, 5.6 cm for C-band) radar pulses is limited, which leads to the detection of the forest canopies rather than the bare land surface. As a result, decorrelation would occur in InSAR analysis, leading to no subsidence results over the densely forested area, as shown in the forest area (Fig. 10), where few pixels (Fig. 11b) obtained subsidence results based on C-band Sentinel-1 images (Fig. 4c and 4e). Penetration capacity can be influenced by forest density as well as forest canopy height (Ni et al. 2014). Therefore, subsidence velocities over the forest area (Fig. 11b) in this study were likely measured from the ground surface over the low-density forest area. Long-wavelength (24.2 cm for L-band, 69.72 cm for P-band) radar pulses have better penetration capacity and can sense further into forest canopies. The calculated subsidence velocities in the forest area (Fig. 11a) based on L-band PALSAR-1

images had relatively large uncertainties (Fig. 4b), likely caused by low coherence (Shirzaei et al. 2020). Besides, a system bias, referred to as the fading signal, has been reported and discussed when multiple multi-looked short temporal baseline interferograms are used to overcome the rapid loss of coherence in long-term interferograms over the forest and densely vegetated areas (Ansari et al. 2021; De Luca et al. 2022; Pepe et al. 2015). This phase bias might be a further possible source of uncertainty in short-time SBAS InSAR analysis.

5.4 Subsidence and Topography Patterns

Topography is essential for flooding risk assessment and management over coastal regions (Miller and Shirzaei 2021). Low-lying coastal areas are more prone to inundation. Subsidence over the low elevation coastal area potentially exacerbates the situation. In this study, subsidence velocities and elevation along the two profiles (Fig. 15a, QI, ST) over the study area were extracted (Fig. 14). Sentinel-1-derived velocities in the vertical direction were higher than PALSAR-1-derived LOS velocities from 2006 to 2011 in the 0 - 12 km section of the profile QI (Fig. 14a). The elevation was lower than 5 m in the QI section 0 - 12 km. Velocities for both sensors increased in QI section 15 - 20 km, where elevation declined nearly 3 m in a similar trend (Fig. 14a). Along with the profile QI, the low elevation area exhibited relatively high velocities, especially during the Sentinel-1 monitoring period. The elevation along the profile ST was relatively lower than QI (Fig. 14b). High velocities appeared in ~5 km, where the elevation was almost lower than 2 m. PALSAR-1 derived LOS

velocities along the ST showed a similar trend to the vertical velocities from Sentinel-1 analysis. By analyzing the subsidence performance over the topographic surface, this study found that some low areas subsided at a relatively high velocity, especially in recent years, which could contribute to flood vulnerability and risk.

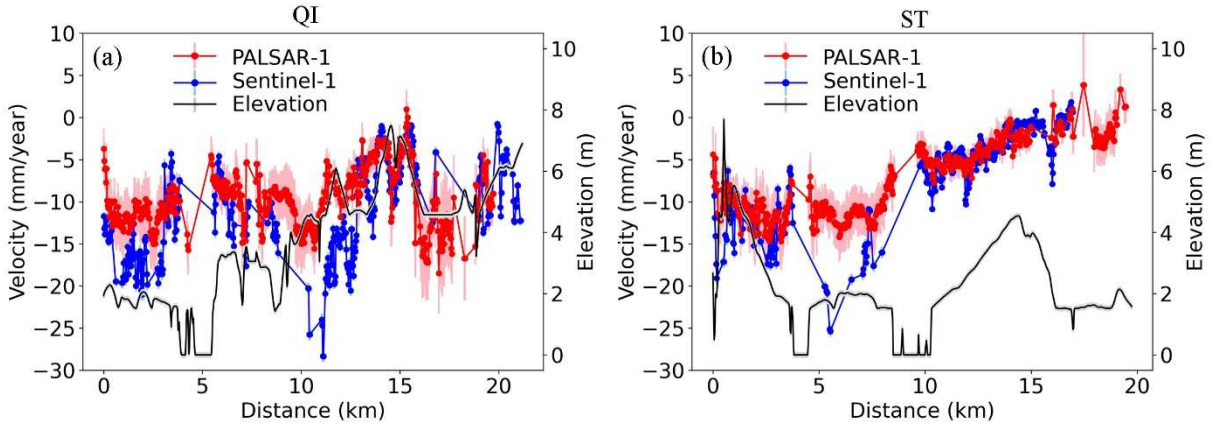

Figure 14. PALSAR-1 LOS velocities from 2006 through 2011 (red line) with standard deviation (pink bar), Sentinel-1 vertical velocities (blue line) with standard deviation (light blue bar), and elevation (black line with vertical accuracy shown as gray bar) along the transects QI and ST. The locations of the transects are shown in Figure 15a.

5.5 Subsidence along Highways

Many low-lying sections of highways are susceptible to flood inundation. Land subsidence could increase their flood vulnerability. This study examined the spatial pattern of subsidence along three highways across the study area (Fig. 15). The highways were digitalized in the Google Earth image and overlaid on the airborne LiDAR-derived DEM (Fig.

652 15a). Changes in elevation along the highway tracks from the northwest to the southeast were
653 illustrated in black (Fig. 15b, 15c, and 15d). Our results demonstrated that variations of
654 PALSAR-1 LOS velocities and Sentinel-1 velocities in the vertical direction along the
655 highway appeared to not correlate with elevation information. In particular, SH 6 underwent a
656 high subsidence velocity (>10 mm/year) over the 0-to-5 km section and lower velocities
657 around -5 mm/year for the rest of the track in both PALSAR-1 and Sentinel-1 results (Fig.
658 15b). Along Gulf Fwy, the estimated subsidence velocities appeared to be stable for the first
659 few kilometers then double from about -5 mm/year to -10 mm/year around the 5 km mark,
660 and then slowly increased for the rest of the track (Fig. 15c). SH 146 experienced high
661 subsidence velocities (~15 mm/year) in the 10-to-15 km section based on Sentinel-1 and
662 PALSAR-1 results (Fig. 15d). However, some low-lying sections of the highways underwent
663 relatively large subsidence velocities, such as around 17 km of the State Highway 6 (SH 6)
664 subsided up to 10mm/year with the elevation below 2 m, around 20 km mark of Gulf Fwy
665 subsided approximately 5-10 mm/year with elevation about 3 m, around 12 km of the State
666 Highway 146 (SH 146) subsided approximately 15 mm/year with elevation about 3 m.
667 Besides, Similar patterns (increasing-to-decreasing velocities along the northwest-southeast
668 direction) were identified in the PALSAR-1 and Sentinel-1 results for all selected highways.

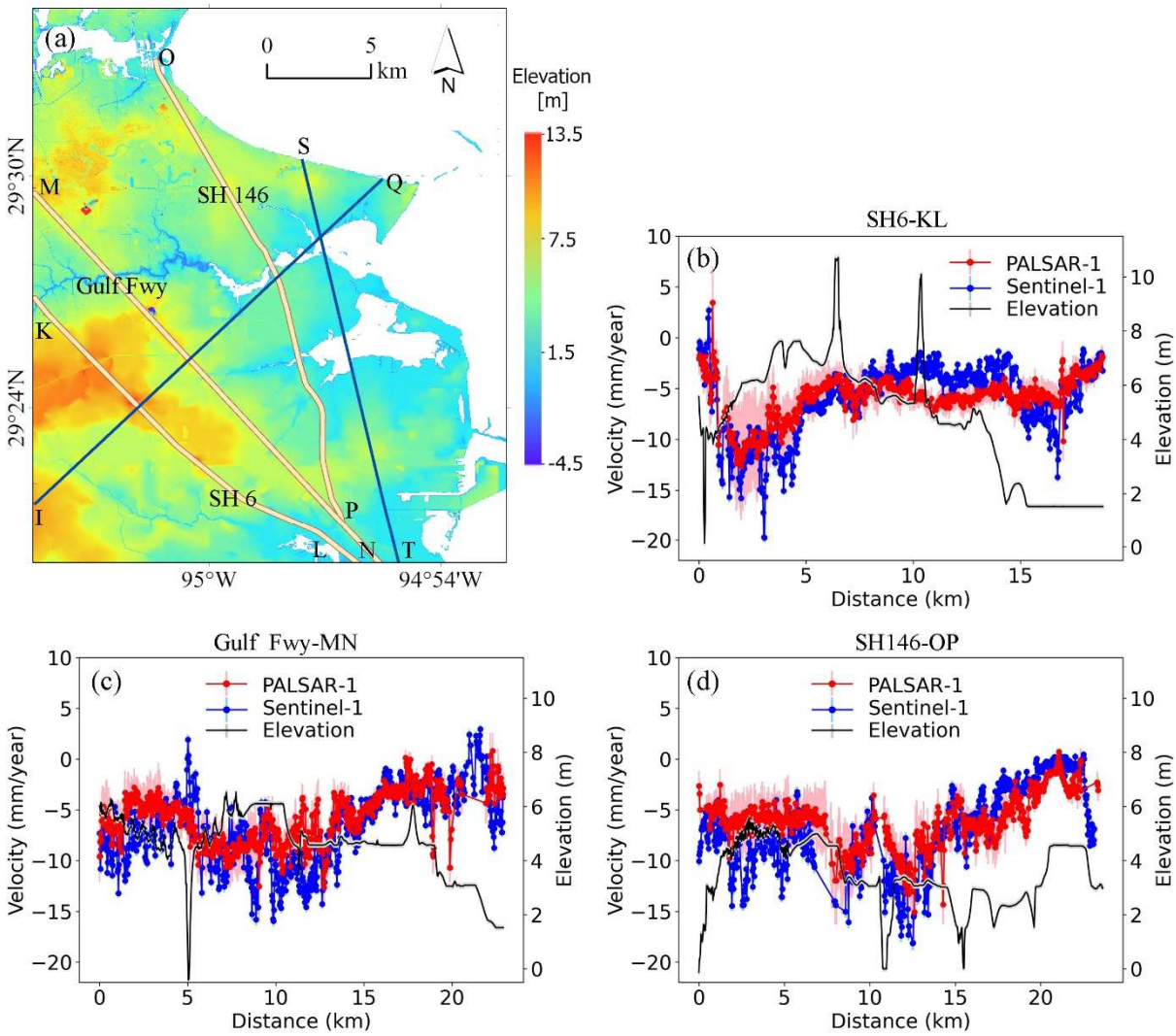

669

670 **Figure 15**. (a) Digitalized highways and selected profiles over the airborne LiDAR-derived
671 DEM. PALSAR-1 LOS velocities (red line) with standard deviation (pink bar), Sentinel-1
672 velocities in the vertical direction (blue line) with standard deviation (light blue bar), and
673 elevation (black line with vertical accuracy shown as gray) over the (b) State Highway 6
674 (SH6)-KL, (c) Gulf Fwy-MN, and (d) State Highway 146 (SH 146)-OP.

675

676 **6. Conclusions**

677 The study integrated SBAS InSAR, airborne LiDAR, and land cover data to investigate
678 coastal subsidence around Eagle Point in Texas, where a high RSLR was recorded at a tide

679 gauge station. Our results revealed that the subsidence velocities were up to −33 mm/year in
680 the LOS direction in 2006-2011 from ALOS-1 PALSAR-1 images and up to −34 mm/year in
681 the vertical direction in 2016-2021 from Sentinel-1 images. The low vertical accuracy of
682 airborne LiDAR measurements has limited its application for land subsidence mapping.
683 However, this study found that airborne LiDAR could be a complementary means to provide
684 information on high-resolution spatial variability of coastal subsidence over the highly
685 subsided area. Our study is unique in terms of using both the InSAR-derived velocities from
686 images time series and LiDAR-derived surface changes from time-lapsed observations.
687 Comparing the InSAR results to 1-m airborne LiDAR measurements showed good agreement
688 along the selected profiles, i.e., areas with higher subsidence velocities based on InSAR
689 tended to have larger surface change based on airborne LiDAR and vice versa. More
690 importantly, the comparison revealed that airborne LiDAR results could be complementary to
691 InSAR results by shedding light on the subpixel variations of InSAR results and identifying
692 significant surface changes that InSAR cannot capture. Airborne LiDAR data are not globally
693 available like SAR images yet, but the availability of airborne LiDAR data is improving
694 rapidly at local or regional levels in many countries. Furthermore, by incorporating land cover
695 data, this study found that the subsidence velocities tended to be higher in forest, grassland,
696 and wetlands than in developed urban areas over the study area. In addition, the subsidence
697 velocities appeared to be negatively correlated with the percent impervious coverage.

698 Overall, the results of this study show that the high vertical accuracy InSAR results and
699 the high spatial resolution airborne LiDAR data could be complementary in subsidence

monitoring. An improved characterization of subsidence using both InSAR and airborne LiDAR results could provide valuable information to support a variety of coastal studies on flood vulnerability, infrastructure reliability, and erosion control. Our findings indicate the need and feasibility of a multi-resolution InSAR-LiDAR fusion for mapping coastal subsidence mapping with both high accuracy and high resolution.

Acknowledgments

We thank four anonymous reviewers and the associate editor for their insightful comments. This work was jointly supported by the National Science Foundation (NSF) under grants 2050986 and 2112631 to Texas A&M University-Corpus Christi, the Conrad Blucher Institute, the U.S. Department of Commerce-National Oceanic and Atmospheric Administration (NOAA) through the University of Southern Mississippi (USM) under the terms of Agreement (No. NA13NOS4000166), and the China Scholarship Council (No. 201906180081). Any opinions, findings, conclusions, or recommendations expressed in this material are those of the authors and do not necessarily reflect the views of NSF, NOAA, USM, and CSC.

References

Ansari, H., De Zan, F., & Parizzi, A. (2021). Study of Systematic Bias in Measuring Surface Deformation With SAR Interferometry. *IEEE Transactions on Geoscience and Remote Sensing, 59*, 1285-1301.

720 Berardino, P., Fornaro, G., Lanari, R., & Sansosti, E. (2002). A new algorithm for surface
721 deformation monitoring based on small baseline differential SAR interferograms. *IEEE*
722 *Transactions on Geoscience and Remote Sensing, 40*, 2375-2383.
723 Blewitt, G., Hammond, W.C., & Kreemer, C. (2018). Harnessing the GPS data explosion for
724 interdisciplinary science. *Eos, 99*, 485.
725 Bürgmann, R., Rosen, P.A., & Fielding, E.J. (2000). Synthetic aperture radar interferometry to
726 measure Earth's surface topography and its deformation. *Annual review of earth and planetary*
727 *sciences, 28*, 169-209.
728 Chen, C.W., & Zebker, H.A. (2002). Phase unwrapping for large SAR interferograms:
729 Statistical segmentation and generalized network models. *IEEE Transactions on Geoscience*
730 *and Remote Sensing, 40*, 1709-1719.
731 Coplin, L.S., & Galloway, D. (1999). Houston-Galveston, Texas. *Land subsidence in the*
732 *United States: US geological survey circular* (pp. 35-48).
733 De Luca, C., Casu, F., Manunta, M., Onorato, G., & Lanari, R. (2022). Comments on "Study of
734 Systematic Bias in Measuring Surface Deformation With SAR Interferometry". *IEEE*
735 *Transactions on Geoscience and Remote Sensing, 60*, 1-5.
736 Dixon, T.H., Amelung, F., Ferretti, A., Novali, F., Rocca, F., Dokka, R., Sella, G., Kim, S.W.,
737 Wdowinski, S., & Whitman, D. (2006). Subsidence and flooding in New Orleans. *Nature, 441*,
738 587-588.

739 Ezer, T., & Atkinson, L.P. (2014). Accelerated flooding along the U.S. East Coast: On the
740 impact of sea-level rise, tides, storms, the Gulf Stream, and the North Atlantic Oscillations.
741 *Earth's Future, 2*, 362-382.
742 Fattahi, H., & Amelung, F. (2015). InSAR bias and uncertainty due to the systematic and
743 stochastic tropospheric delay. *Journal of Geophysical Research: Solid Earth, 120*, 8758-8773
744 Ferretti, A., Prati, C., & Rocca, F. (2001). Permanent scatterers in SAR interferometry. *IEEE*
745 *Transactions on Geoscience and Remote Sensing, 39*, 8-20.
746 Fialko, Y., & Simons, M. (2001). The complete (3-D) surface displacement field in the
747 epicentral area of the 1999MW7.1 Hector Mine Earthquake, California, from space geodetic
748 observations. *Geophysical Research Letters, 28*, 3063-3066.
749 Frederikse, T., Landerer, F., Caron, L., Adhikari, S., Parkes, D., Humphrey, V.W., Dangendorf,
750 S., Hogarth, P., Zanna, L., Cheng, L., & Wu, Y.H. (2020). The causes of sea-level rise since
751 1900. *Nature, 584*, 393-397.
752 Global Ocean Commission (2014). From decline to recovery: A rescue package for the global
753 ocean. *Global Ocean Commission.*
754 Higgins, S.A., Overeem, I., Steckler, M.S., Syvitski, J.P.M., Seeber, L., & Akhter, S.H. (2014).
755 InSAR measurements of compaction and subsidence in the Ganges-Brahmaputra Delta,
756 Bangladesh. *Journal of Geophysical Research: Earth Surface, 119*, 1768-1781.
757 Huang, B., Shu, L., & Yang, Y.S. (2012). Groundwater Overexploitation Causing Land
758 Subsidence: Hazard Risk Assessment Using Field Observation and Spatial Modelling. *Water*
759 *Resources Management, 26*, 4225-4239.

760 Jin, S., Homer, C., Yang, L., Danielson, P., Dewitz, J., Li, C., Zhu, Z., Xian, G., & Howard, D.
761 (2019). Overall Methodology Design for the United States National Land Cover Database 2016
762 Products. *Remote Sensing, 11*, 2971.
763 Jolivet, R., Grandin, R., Lasserre, C., Doin, M.P., & Peltzer, G. (2011). Systematic InSAR
764 tropospheric phase delay corrections from global meteorological reanalysis data. *Geophysical*
765 *Research Letters, 38*, L17311.
766 Jones, B.M., Stoker, J.M., Gibbs, A.E., Grosse, G., Romanovsky, V.E., Douglas, T.A.,
767 Kinsman, N.E.M., & Richmond, B.M. (2013). Quantifying landscape change in an arctic
768 coastal lowland using repeat airborne LiDAR. *Environmental Research Letters, 8.*
769 Leatherman, S.P., Zhang, K., & Douglas, B.C. (2000). Sea level rise shown to drive coastal
770 erosion. *Eos, Transactions American Geophysical Union, 81*, 55-57.
771 Liu, Y., Li, J., Fasullo, J., & Galloway, D.L. (2020). Land subsidence contributions to relative
772 sea level rise at tide gauge Galveston Pier 21, Texas. *Scientific Reports, 10*, 1-11.
773 May[1], N.C., & Toth, C.K. (2007). Point positioning accuracy of airborne LiDAR systems: A
774 rigorous analysis. *International Archives of Photogrammetry, Remote Sensing and Spatial*
775 *Information Sciences, Munich, Germany*, 19-21.
776 Meredith, M., M. Sommerkorn, S. Cassotta, C. Derksen, A. Ekaykin, A. Hollowed, G. Kofinas,
777 A. Mackintosh, J. Melbourne-Thomas, M.M.C. Muelbert, G. Ottersen, H. Pritchard, & E.A.G.
778 Schuur. (2019). Polar Regions. IPCC Special Report on the Ocean and Cryosphere in a
779 Changing Climate.
780

781 Miller, M.M., & Shirzaei, M. (2019). Land subsidence in Houston correlated with flooding
782 from Hurricane Harvey. *Remote Sensing of Environment, 225*, 368-378.
783 Miller, M.M., & Shirzaei, M. (2021). Assessment of Future Flood Hazards for Southeastern
784 Texas: Synthesizing Subsidence, Sea-Level Rise, and Storm Surge Scenarios. *Geophysical*
785 *Research Letters, 48*, 2021GL092544.
786 Neumann, B., Vafeidis, A.T., Zimmermann, J., & Nicholls, R.J. (2015). Future coastal
787 population growth and exposure to sea-level rise and coastal flooding-a global assessment.
788 *PLoS One, 10*, e0118571.
789 Ni, W., Zhang, Z., Sun, G., Guo, Z., & He, Y. (2014). The Penetration Depth Derived from the
790 Synthesis of ALOS/PALSAR InSAR Data and ASTER GDEM for the Mapping of Forest
791 Biomass. *Remote Sensing, 6*, 7303-7319.
792 Okyay, U., Telling, J., Glennie, C.L., & Dietrich, W.E. (2019). Airborne lidar change detection:
793 An overview of Earth sciences applications. *Earth-Science Reviews, 198.*
794 Pepe, A., Yang, Y., Manzo, M., & Lanari, R. (2015). Improved EMCF-SBAS Processing Chain
795 Based on Advanced Techniques for the Noise-Filtering and Selection of Small Baseline
796 Multi-Look DInSAR Interferograms. *IEEE Transactions on Geoscience and Remote Sensing,*
797 *53*, 4394-4417.
798 Qu, F., Lu, Z., Zhang, Q., Bawden, G.W., Kim, J.-W., Zhao, C., & Qu, W. (2015). Mapping
799 ground deformation over Houston–Galveston, Texas using multi-temporal InSAR. *Remote*
800 *Sensing of Environment, 169*, 290-306.

801 Rosen, P.A., Gurrola, E., Sacco, G.F., & Zebker, H. (2012). The InSAR scientific computing
802 environment. In, *EUSAR 2012; 9th European conference on synthetic aperture radar* (pp.
803 730-733): VDE.
804 Schuerch, M., Spencer, T., Temmerman, S., Kirwan, M.L., Wolff, C., Lincke, D., McOwen,
805 C.J., Pickering, M.D., Reef, R., Vafeidis, A.T., Hinkel, J., Nicholls, R.J., & Brown, S. (2018).
806 Future response of global coastal wetlands to sea-level rise. *Nature, 561*, 231-234.
807 Shirzaei, M., Freymueller, J., Törnqvist, T.E., Galloway, D.L., Dura, T., & Minderhoud, P.S.J.
808 (2020). Measuring, modelling and projecting coastal land subsidence. *Nature Reviews Earth &*
809 *Environment, 2*, 40-58.
810 Trepekli, K., Balstrøm, T., Friborg, T., Fog, B., Allotey, A.N., Kofie, R.Y., & Møller-Jensen, L.
811 (2022). UAV-borne, LiDAR-based elevation modelling: a method for improving local-scale
812 urban flood risk assessment. Natural Hazards, 1-29.
813 Wang, G., Turco, M., Soler, T., Kearns, T.J., & Welch, J. (2017). Comparisons of OPUS and
814 PPP Solutions for Subsidence Monitoring in the Greater Houston Area. *Journal of Surveying*
815 *Engineering, 143*, 05017005.
816 Wang, H., Wright, T.J., Yu, Y., Lin, H., Jiang, L., Li, C., & Qiu, G. (2012). InSAR reveals
817 coastal subsidence in the Pearl River Delta, China. *Geophysical Journal International, 191*,
818 1119-1128.
819 Wickham, J., Stehman, S.V., Sorenson, D.G., Gass, L., & Dewitz, J.A. (2021). Thematic
820 accuracy assessment of the NLCD 2016 land cover for the conterminous United States. *Remote*
821 *Sensing of Environment, 257*, 112357.

822 Wright, T.J., Parsons, B.E., & Zhong, L. (2004). Toward mapping surface deformation in three
823 dimensions using InSAR. *Geophysical Research Letters, 31.*
824 Xu, Y., Lu, Z., & Kim, J.-W. (2021). P-Band InSAR for Geohazard Detection over Forested
825 Terrains: Preliminary Results. *Remote Sensing, 13*, 4575.
826 Yunjun, Z., Fattahi, H., & Amelung, F. (2019). Small baseline InSAR time series analysis:
827 Unwrapping error correction and noise reduction. *Computers & Geosciences, 133*, 104331.
828

List of Figure Captions

Figure 1. Study area: (a) SAR data coverage (black squares) over the elevation map around the study area (red square); (b) a Google Earth image of the study area and the monthly mean RSLR observed at the Eagle Point Tide Gauges Station (blue marker) from 1993 to 2017. Red marker shows the location of the TXLM GPS station, and magenta dots denote the location of the reference points for Sentinel-1 and ALOS-1 PALSAR-1 image processing.

Figure 2. Research framework.

Figure 3. Interferogram networks from ALOS-1 PALSAR-1 and Sentinel-1 acquisitions with the perpendicular and temporal baselines: (a) PALSAR-1 ascending images, (b) Sentinel-1 ascending images, and (c) Sentinel-1 descending images. Red circles represent SAR images.

Figure 4. LOS velocities and standard deviations derived from (a and b) PALSAR-1 ascending images (2006-2011), (c and d) Sentinel-1 Path 136 ascending images (2016-2021), and (e and f) Sentinel-1 Path 143 descending images (2016-2021).

Figure 5. The vertical components under the assumption of zero north-south motion in 2016-2021 based on Sentinel-1 ascending and descending LOS results (Fig. 4c and 4e).

850 **Figure 6**. Comparison of InSAR-derived cumulative subsidence to GPS measurements in the
851 vertical direction. The location of the TXLM GPS station is shown in Figure 1.
852
853 **Figure 7.** Detailed subsidence pattern of a selected area: (a) Google Earth image, (b) airborne
854 LiDAR-derived vertical surface differences, (c) vertical component based on PALSAR-1
855 results (assuming no east-west and north-south motions), and (d) vertical component based on
856 Sentinel-1 results (assuming no north-south motion). Figure 1b shows the location of this
857 area.
858
859 **Figure 8.** Comparison of InSAR and airborne LiDAR results along transect lines L1 (a and b)
860 and L2 (c and d). Error bars indicate standard deviations. The locations of the transect lines
861 are shown in Figure 7a.
862
863 **Figure 9.** Historical Google Earth images and airborne LiDAR-derived land surface
864 differences over the selected profiles BC (a) and HI (b). The locations of BC and HI are
865 shown in Fig. 7a.
866 Checkpoints B, C, H, and I are denoted by yellow placemarks.
867
868 **Figure 10**. Land cover of the study area based on NLCD 2019.
869

870 **Figure 11**. PALSAR-1 mean LOS velocities (a) and Sentinel-1 mean vertical velocities (b) for
871 different land cover types. The 95% confidence intervals are computed as 1.96 standard errors
872 for each land type. The red line represents the number of pixels. Subplots c and d show the
873 interquartile ranges of PALSAR-1 LOS velocities and Sentinel-1 vertical velocities for
874 different land cover types, respectively.
875
876 **Figure 12**. Relationships between percent impervious coverage and subsidence velocities:
877 PALSAR-1 LOS velocities at (a) the pixel level and (b) the cluster level; Sentinel-1 vertical
878 velocities at (c) the pixel level and (d) the cluster level. Black lines (a and c) and red lines (b and
879 d) indicate linear fit.
880
881 **Figure 13.** Examples of the multiscale measurements: (a) a grassland area (dashed box) with
882 details presented in the second row; and (b) a developed area (solid box) with details
883 presented in the third row. In example (a), the 0.3-m HxGN aerial image shows the landscape.
884 In example (b), black arrows indicate the ditch and the culvert. This area is also marked in
885 Figure 7b.
886
887 **Figure 14**. PALSAR-1 LOS velocities from 2006 through 2011 (red line) with standard
888 deviation (pink bar), Sentinel-1 vertical velocities (blue line) with standard deviation (light blue
889 bar), and elevation (black line with vertical accuracy shown as gray bar) along the transects QI
890 and ST. The locations of the transects are shown in Figure 15a.

891

892 **Figure 15**. (a) Digitalized highways and selected profiles over the airborne LiDAR-derived
893 DEM. PALSAR-1 LOS velocities (red line) with standard deviation (pink bar), Sentinel-1
894 velocities in the vertical direction (blue line) with standard deviation (light blue bar), and
895 elevation (black line with vertical accuracy shown as gray) over the (b) State Highway 6
896 (SH6)-KL, (c) Gulf Fwy-MN, and (d) State Highway 146 (SH 146)-OP.